

Article

Artificial Intelligence Monitoring of Hardening Methods and Cutting Conditions and Their Effects on Surface Roughness, Performance, and Finish Turning Costs of Solid-State Recycled Aluminum Alloy 6061 Chips

Adel Taha Abbas ^{1,*} , Danil Yurievich Pimenov ² , Ivan Nikolaevich Erdakov ³, Mohamed Adel Taha ⁴, Magdy Mostafa El Rayes ¹ and Mahmoud Sayed Soliman ¹

¹ Department of Mechanical Engineering, College of Engineering, King Saud University, P.O. Box 800, Riyadh 11421, Saudi Arabia; melrayes@ksu.edu.sa (M.M.E.R.); solimanm@ksu.edu.sa (M.S.S.)

² Department of Automated Mechanical Engineering, South Ural State University, Lenin Prosp. 76, Chelyabinsk 454080, Russia; danil_u@rambler.ru

³ Foundry Department, South Ural State University, Lenin Prosp. 76, Chelyabinsk 454080, Russia; wissenschaftler@bk.ru

⁴ Department of Mechanical Design and Production, Faculty of Engineering, Zagazig University, Zagazig 44519, Egypt; eng_mohamed_2017@yahoo.com

* Correspondence: aabbas@ksu.edu.sa

Received: 27 April 2018; Accepted: 21 May 2018; Published: 29 May 2018



Abstract: Aluminum Alloy 6061 components are frequently manufactured for various industries—aeronautics, yachting, and optical instruments—due to their excellent physical and mechanical properties, including corrosion resistance. There is little research on the mechanical tooling of AA6061 and none on its structure and properties and their effects on surface roughness after finish turning. The objective of this comprehensive study is, therefore, to ascertain the effects of both the modern method of hardening AA6061 shafts and the finish turning conditions on surface roughness, R_a , and the minimum machining time for unit-volume removal, T_m , while also establishing the cost price of processing one part, C . The hardening methods improved both the physical and the mechanical material properties processed with 2, 4, and 6 passes of equal channel angular pressing (ECAP) at room temperature, using an ECAP-matrix with a channel angle of 90° . The reference workpiece sample was a hot extruded chip under an extrusion ratio (ER) of 5.2 at an extrusion temperature of 500°C ($ET = 500^\circ\text{C}$). The following results were obtained: grain size in ECAP-6 decreased from 15.9 to $2.46\ \mu\text{m}$, increasing both microhardness from 41 Vickers hardness value (HV) to 110 HV and ultimate tensile strength from 132.4 to $403\ \text{MPa}$. The largest decrease in surface roughness, R_a —70%, was obtained turning a workpiece treated with ECAP-6. The multicriteria optimization was computed in a multilayer perceptron-based artificial neural network that yielded the following optimum values: the minimal length of the three-dimensional estimates vector with the coordinates $R_a = 0.800\ \mu\text{m}$, $T_m = 0.341\ \text{min}/\text{cm}^3$, and $C = 6.955\ \$$ corresponded to the optimal finish turning conditions: cutting speed $v_c = 200\ \text{m}/\text{min}$, depth of cut $a_p = 0.2\ \text{mm}$, and feed per revolution $f_r = 0.103\ \text{mm}/\text{rev}$ (ET-500 extrusion without hardening).

Keywords: artificial neural network; equal channel angular pressing; extrusion; recycled aluminum alloy 6061 chips; turning operation; optimization; surface roughness

1. Introduction

Turning is widely used today in car manufacturing, machine, and machine-tool building as well as in other industries. One essential quality parameter in finish turning [1–7], milling [8–12], grinding [13–15] is surface roughness, Ra . There are many promising modern materials, such as Aluminum Alloy 6061 that is a frequent industrial component for aeronautics, yachting, and optical instruments. Nonetheless, the problem of designing the optimal turning conditions, considering both the physical and the mechanical improvements in material properties after 2, 4, and 6 equal channel angular pressing (ECAP) passes of the alloy is a novel area of study. Microstructural refinement of AA6061 contributes both to the tensile strength and to the microhardness of its material properties. Alloy 6061 is one of the most widely used 6000 series alloys. This standard structural alloy is one of the most versatile heat-treated alloys, popular for high and medium impact applications, with good impact resistance. Alloy 6061 has excellent corrosion resistance in ambient conditions and good corrosion resistance in seawater, good finishing characteristics [16], and it reacts well to anodizing, welding, and various commercial methods of coupling. Lazzaro and Atzori [17] demonstrated that Alloy 6061 has adequate machinability characteristics in the heat-treated condition. Conventional recycling requires melting of the scrap, which is characterized by high-operating costs, high energy consumption, and a large number of operations. On the other hand, solid-state recycling is the recycling of scrap with no re-melting, to avoid the disadvantages of the conventional method. Gronostajski and Matuszak [18] argued that solid-state recycling of aluminum chips, if compared to conventional recycling, can minimize losses and energy consumption by up to 40% and 31%, respectively. However, there is virtually no research on establishing the optimum turning conditions for AA6061 workpieces improved with ECAP 2, 4, and 6. Both surface quality and the use of minimal resources are equally important in the machining of expensive materials such as Alloy 6061. So, the design surface roughness, Ra , has to be established at a minimum machining time of unit volume, T_m , and at a minimum machining cost, C , for various grades of aluminum alloy 6061 with ECAP 2, 4, and 6, given a workpiece produced by chip extrusion at 500 °C (extrusion temperature (ET) = 500 °C).

Models for predicting surface roughness in turning are widely researched [19–39]. Risbood et al. [19] determined that surface roughness, Ra , can be predicted with reasonable accuracy using an artificial neural network and taking the radial vibration acceleration of the tool holder as feedback. Svalina et al. [20] applied neural networks in their analysis of cutting conditions and their effect on surface roughness, by comparing the prediction function values with the surface roughness results. Asiltürk [21] used artificial neural networks (ANN) and multiple regression methods (MRM) to develop models for predicting the surface roughness of AISI 1040 steel material. Azam et al. [22] developed an average surface roughness (Ra) model for turning high-strength low-alloy AISI 4340 steel using multilayer coated carbide tools. Acayaba and Escalona [23] used experimental data in their surface roughness prediction modeling of low-speed turning of AISI 316 austenitic stainless steel, using multiple linear regression and ANN. Mia and Dhar [24] presented a predictive model of average surface roughness in the turning of hardened EN 24T steel, using an ANN and Matlab software. Nieslony et al. [25] presented the problem of precise turning of the molded parts with variable compliance and presented a topographic inspection of the machined surface quality. Jurkovic et al. [26] studied surface roughness (Ra), cutting force (F_c), and tool lifetime (T) in high-speed turning, by applying three machine learning methods for the prediction of independent output cutting parameters. Mia et al. [27] studied the effect of three sustainable techniques and the traditional flood cooling system, on prominent machining indices such as cutting temperature, surface roughness, chip characteristics, and tool wear in plain turned hardened AISI 1060 steel. However, none of the above studies [19–27] included models for predicting surface roughness in the turning of Alloy 6061.

Sreejith [28] reported the influence of various lubricants on cutting forces, machined surface roughness, and tool wear in the turning of a 6061-aluminum alloy with a diamond-coated carbide tool. Anandkrishnan and Mahamani [29] presented the results of an experimental investigation into the in situ machinability of an Al-6061-TiB₂ metal matrix composite (MMC) prepared by

flux-assisted synthesis. They demonstrated that an increase in feed rate produced higher tool wear, surface roughness, and that it minimized the cutting forces. Ter Horst et al. [30] presented the results of diamond turning and polishing of aluminum alloys 6061 T6 and showed the potential of these new alloys with surface roughness values of 1 nm on RSA 6061 and RSA 708. Islam [31] presented the experimental and the analytical results of an investigation into additional factors that affected the dimensional accuracy and surface roughness, Ra , of turned aluminum 6061, mild steel 1030, and alloy steel 4340 workpieces, as well as the three major cutting parameters—cutting speed, feed rate, and depth of cut. Cheng et al. [32,33] discussed diamond turnability characteristics and coating processes for both traditional aluminum 6061 and RSA. Kalyan and Samuel [34] established a set of cutting modes based on the machining forces, surface roughness and chip morphology at varying cutting-edge chamfer widths in the high speed turning of an AlMgSi (Al 6061 T6) alloy, using polycrystalline diamond (PCD) tools. Mkoko and Abou-El-Hossein [35] observed the effects of depth of cut and feed rate at a fixed rotational speed on tool-wear rates and the resulting surface roughness of specimens turned with a diamond cutting tool from an aluminum alloy (6061-T6). Davoudinejad et al. [36] investigated tool life and tool wear mechanisms, as well as evaluating surface roughness in various conditions of dry orthogonal cutting of Al6061. Davoudinejad et al. [37] presented the effect of various cutting speeds in the turning of Al6061, with regard to different coatings. Hiremath et al. [38] studied the influence of various cutting conditions on cutting forces and surface roughness in the turning of 6061Al on a conventional lathe machine using a PCD tool. Tootooni et al. [39] used non-contact, vision-based online measurement for investigating surface finish in the turning of external steel and aluminum-alloy shaft diameters (4340 and 6061 grades). A number of studies [28–39] have investigated the turning of 6062 aluminum alloys. However, none accounted for the physical and mechanical properties attributed to the various conditions of the AA6061 workpiece on surface roughness in turning. In addition, the models for predicting or establishing surface roughness presented in studies [19–39] in no case established the cutting conditions that would yield optimum surface roughness.

Turning now to the papers that have described the establishment of optimum surface roughness in turning [40–46], Zuperl and Cus [40] proposed a neural network-based approach to complex optimization of cutting parameters, considering technological, economic, and organizational limitations. Gupta et al. [41] focused on process parameter optimization in turning operations: surface roughness, flank tool wear, and required power using an ANN integrated with a genetic algorithm (GA). Bouacha and Terrab [42] investigated and optimized hard turning of AISI 52100 bearing steel with a cubic boron nitride (CBN) tool. The combined effects of the process parameters (cutting speed, feed rate, depth of cut, cutting time, and workpiece hardness) on performance characteristics (tool wear, surface roughness, and cutting forces) were studied with analysis of variance (ANOVA). Mia et al. [43] presented an optimization of cutting forces, average surface roughness, cutting temperature, and chip reduction coefficients in the turning of an Ti-6Al-4V alloy. However, no cutting conditions were investigated in the above studies [40–43] in relation to the optimum surface roughness of a turned aluminum alloy 6061. Bataineh and Dalalah [44] proposed a strategy for optimizing the cutting parameters of dry turned aluminum alloys (6061-T6), to improve surface roughness and machining time and to minimize machining costs. Abbas et al. [45] investigated surface roughness in the turning of solid-state recycled aluminum alloy 6061 chips. Ragab et al. [46] investigated the effect of extrusion temperature and turning parameters on the surface roughness of aluminum alloys 6061. However, studies [40–45] provided only a one-sided interpretation of the problem of estimating the optimum cutting conditions by taking surface roughness into consideration, but not its correlation with the unit volume machining time, T_m , and the cost of machining, C , which is unacceptable in the machining of materials as expensive as an aluminum alloy 6061.

Considering the above, if we look at the studies describing the establishment of the optimum turning conditions using multi-objective optimization [47–52], Basak et al. [47] presented two types of Pareto optimization of a hard turning process for the machining of D2 steel with ceramic tools. The goal

was to minimize machining time and cost. Rather than a constraint, tool life was an integral part of the surface roughness calculation. Karpat and Özel [48] used the Pareto method for optimizing machining conditions in the longitudinal turning of hardened AISI H13 steel, minimizing surface roughness values and maximizing productivity, tool life, and material removal rate, and minimizing machine-induced surface stresses. Yue et al. [49] established a correlation between surface roughness, plastic deformation thickness, and cutting conditions in the hard turning of die steel (Cr12MoV) using multi-objective Pareto optimization. Abbas et al. [50,51] used Pareto optimization to establish the turning conditions of a heat-treated alloy steel material (J-Steel), for the minimization of surface roughness, and the turning conditions of a high-strength steel machining time, for the removal of a unit volume. Abbas et al. [52] studied surface roughness, Ra , minimum unit-volume machining time, T_m , cost of processing one part, C , in magnesium alloy AZ61 finish turning. Papers on multi-objective optimization in turning are, therefore, not very numerous. The Pareto method is the most efficient method for solving these sorts of tasks. However, no multicriterion optimization of Alloy 6061 machining was proposed in the above studies [37–52]. Moreover, these studies took no account of the physical and the mechanical properties of the various conditions of the AA6061 workpiece on surface roughness in turning. Considering the high cost of this material, it is necessary to guarantee the design value of surface roughness and minimum machining time at the minimum cost of machining.

In this study, the objective is to study hardening methods and cutting conditions when turning the AA6061 alloy workpiece and their influence on surface roughness (Ra) in finish turning, on machining time for unit volume removal (T_m), and on the cost price of processing one part (C) with artificial intelligence (AI) techniques.

To do so, the following tasks have to be solved:

- Investigation of hardening methods and cutting conditions when turning an AA6061 alloy workpiece and their influence on Ra , T_m , and C using a three-dimensional estimates vectors and AI;
- Study of the effects of a dynamic hardening method on the microstructure and the properties of an AA6061 alloy workpiece;
- Assembly of ANNs in the form of multilayer perceptron with a high prediction accuracy for the prediction of Ra , T_m , and C ;
- Definition of dynamic hardening methods applied to an AA6061 alloy workpiece and their influence on the limits of Ra , T_m , and C ;
- Definition of optimum cutting conditions in the turning of an AA6061 alloy workpiece.

2. Materials, Methods and Experiments

The chemical composition of the aluminum alloy (AA6061 received as an extruded rod) under study is shown below in Table 1. Machined chips of the as-received rod were dry turned under the following cutting conditions: cutting speed 88 m/min, feed 1 mm/rev, and depth of cut, 1 mm. The chips were cold-compacted at room temperature in a 25 mm die, followed by hot extrusion at a temperature of 500 °C and an extrusion ratio of 5.2. The samples were subjected to up to six ECAP passes at room temperature, which improved the properties of the extruded samples, using an ECAP channel die angle (Φ) of 90°.

Table 1. Chemical composition of aluminum alloy AA6061.

Si	Mg	Fe	Cu	Mn	Others	Al
0.8	0.85	0.48	0.26	0.051	0.329	Balance

ECAP is at present one of the recently developed severe plastic deformation (SPD) techniques. Grain refinement is achieved by imposing severe shear strain on samples extruded through a die with

an equal channel bent at an arbitrary angle, as shown in Figure 1. There are two main angles Φ and Ψ , referred to as the internal channel angle and outer radius angle, respectively [53]. The advantage of this process is that large uniform plastic strain can be imposed repeatedly on samples without any change in the cross-sectional dimensions. Moreover, ECAP can be used for the consolidation of composites at relatively low temperatures, leading to improvements in phase distribution reinforcement and the removal of porosities [54].

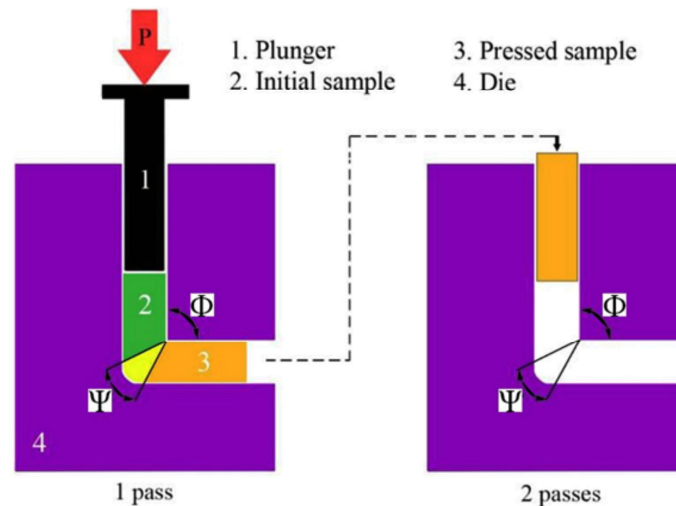


Figure 1. Schematic diagram of the equal channel angular pressing (ECAP) process [53].

Ground, polished, and etched metallographic specimens were prepared using Keller's reagent. A Zeiss Axio Imager (Zeiss, Oberkochen, Germany) microscopy-generated images of the as-received and extruded specimens. Following ECAP, an FEI INSPECT S50 scanning electron microscope (SEM) (FEI, Tokyo, Japan) generated the images for examination, because of the expected fine microstructure. Vickers microhardness under an applied loading of 100 gf and a dwell time of 15 s was measured with a Buehler Micromet 5100 (Buehler, Orlando, FL, USA) at room temperature. A LR300K (300 kN) universal testing machine (Instron, Tokyo, Japan) tested sample tensility at room temperature, at an initial strain rate of $8.33 \times 10^{-4} \text{ s}^{-1}$. The specimens were prepared in accordance with ASTM-B557-06.

Machining of the processed billets was done with an Emco Concept Turn 45 CNC lathe (Emco, Salzburg, Austria), fitted with a Sinumeric 840-D digital NC system. All test runs used a CNC part program. The specifications of both the tool holder and the insert were SVJCL2020K16 and VCGT160404 FN-ALU, respectively. The clearance angle, cutting edge angle, and nose radius were, respectively, held at 5° , 35° and 0.4 mm. The digital NC system controlled all cutting parameters through a CNC part program. The experiments were all conducted under wet conditions. A TESA surface roughness tester was used (TESA, Lausanne, Switzerland) to evaluate surface roughness. The diameter and the length of the test specimens were, respectively, 11 mm and 100 mm. The test specimens were divided into six areas. The first area with a length of 40 mm was used for chuck clamping, the other four areas, each measuring 10 mm, separated by a groove of 2 mm, was used for random machining at various cutting parameters, and the last area was used for centering. A drawing of the test specimen is shown in Figure 2. The test specimens had four different starting conditions; hot extruded at 500°C and ECAP at up to six passes. The cutting parameters, surface roughness values, R_a , and machining time for unit volume removal, T_m , are listed in Table 2 and Tables 5–8. Where, R_a , is the arithmetic average deviation of the assessed profile (μm) and T_m is the machining time for removal of a unit volume (min/cm^3) from an AA6061 alloy workpiece.

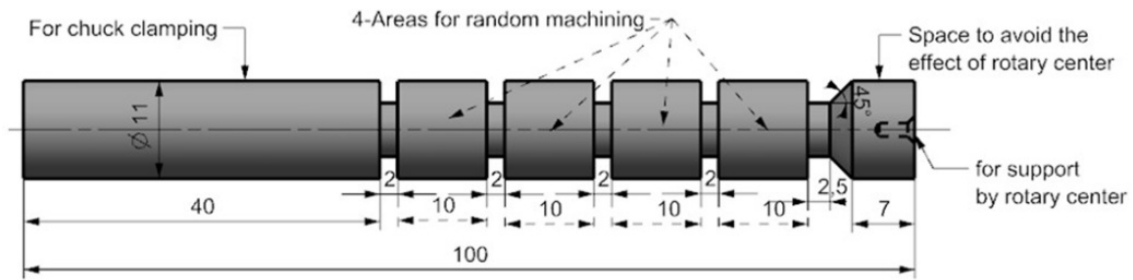


Figure 2. Test specimen drawing (unit: mm).

Table 2. A selection of surface roughness values listed under different cutting conditions.

Cutting Speed: v_c , (m/min)	Feed: f_r , (mm/rev)	Surface Roughness: R_a (μm)			
		Depth of Cut: a_p , (mm)			
		0.25	0.5	0.75	1.0
100	0.0400	0.1730	0.1660	0.1500	0.1290
100	0.0800	0.3880	0.3610	0.3530	0.4400
100	0.1200	0.8720	0.9520	1.0470	1.0200
100	0.1600	1.6780	2.1040	2.1790	2.6290
150	0.0400	0.1460	0.1320	0.1160	0.1890
150	0.0800	0.3440	0.3480	0.3150	0.4130
150	0.1200	0.9310	1.0540	0.9840	0.9990
150	0.1600	1.6370	1.7640	1.7020	1.8840
200	0.0400	0.1820	0.1800	0.2040	0.1500
200	0.0800	0.3670	0.3860	0.3970	0.3550
200	0.1200	0.8450	1.0240	1.0340	1.2140
200	0.1600	1.9760	1.9220	1.9350	2.0140
250	0.0400	0.1230	0.1830	0.1370	0.2240
250	0.0800	0.3590	0.3890	0.3580	0.3250
250	0.1200	0.9370	0.9680	0.9500	1.0000
250	0.1600	2.0880	1.9540	2.0170	1.8930

A fragment of surface roughness values for the different cutting conditions is presented in Table 2. The full listing includes 420 measurements for discrete ranges of values: [100 ÷ 200]—cutting speed, v_c , m/min; [0.1 ÷ 0.4]—depth of cut, a_p , mm; [0.012 ÷ 0.15]—feed, f_r , mm/rev. The listing of all the specimens produced and the corresponding results are detailed in Tables 5–8.

The basic economic parameters for optimizing the turning of an AA6061 aluminum alloy workpiece are summarized below, in Table 3.

Table 3. Summary of basic economic parameters.

No.	Cost of Machining/Hour (SR 400), CMh : \$	Cost of Tool Holder, C_{Toolh} : \$	Tool Holder Life: LT_{Toolh} min	Cost of Insert, C_{In} : \$	Setup Insert: k	Unit Cost of Work-Piece: C_w : \$	Tool Life: T min	Cost of Tool Minute: $C_{Toolmin}$, \$
ET500 °C						7		
ECAP-2	106	85	2,628,000	10	2	12	60	0.083
ECAP-4						16		
ECAP-6						20		

In Table 3 the parameters LT_{Toolh} and $C_{Toolmin}$ are calculated according to the formulas:

$$LT_{Toolh} = 5 \text{ Year} \times 365 \text{ Day} \times 24 \text{ h} \times 60 \text{ min} = 2,628,000 \text{ min}; \tag{1}$$

$$C_{Toolmin} = (C_{In}/(T \times k)) + (C_{Toolh} \times LT_{Toolh}) = 0.083 \text{ $}. \tag{2}$$

The microstructure of the as-received sample is shown in Figure 3a. It consisted of a coarse-grained structure with a grain size of approximately 48 μm . In contrast, the microstructure of the hot extruded specimen consisted of fine grains of about 15.9 μm , as shown in Figure 3b. The finer grained microstructure was caused by severe plastic strain imposed during the recycling processes and the positive effect of chip boundaries, which can act as barriers between grains to prevent grain growth [55–57]. SEM micrographs of samples that had undergone ECAP after 2 and 6 passes are shown in Figure 3c,d, respectively. The incremental grain refinement at increasing numbers of ECAP passes is evident. ECAP sample grain sizes processed after 2 and 6 passes were 5 and 2.46 μm , respectively.

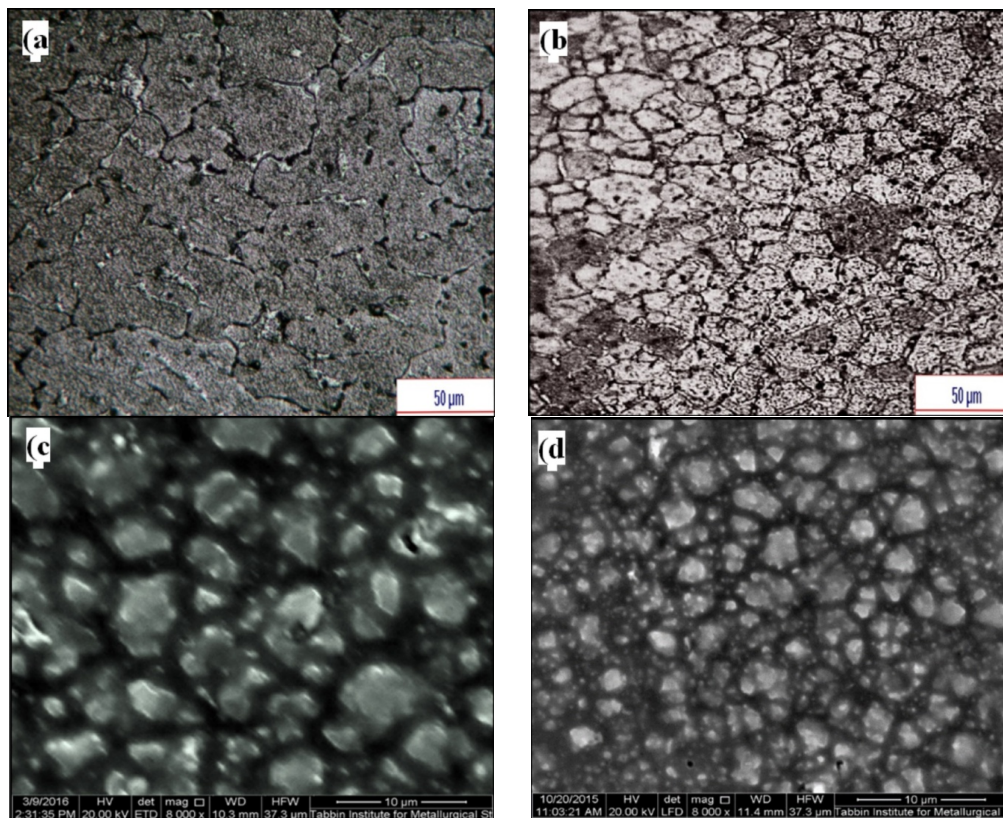


Figure 3. Microstructure of as-received (a) extrusion temperature (ET) = 500 °C; (b) ECAP-2; (c) ECAP-4; and (d) ECAP-6.

Table 4 presents the relative density, microhardness, ultimate tensile strength, and grain size of the solid state recycled aluminum Alloy 6061 chips following extrusion and ECAP processing of the extruded billet after two, four, and six passes. The values presented in Table 4 for the properties of the solid-state recycled billets are indicators of successful recycling of the chips into consolidated bulk materials via cold compaction, followed by hot extrusion, and finally ECAP. Table 4 shows the effects of the number of ECAP passes on the microhardness of the recycled samples. Microhardness increased from 41 HV after extrusion to about 110 HV when extrusion was coupled with ECAP at 6 passes. Similar observations of ultimate tensile strength that increased from 132.4 to 403 MPa were also noted. The drastic increase in mechanical strength was mainly due to the high dislocation density and grain refinement associated with severe deformation accompanied with ECAP. Room temperature ECAP deformation also improved relative density. The increase in mechanical strength was expected to have a significant effect on surface roughness.

Table 4. Effect of ECAP process on solid-state recycled aluminum Alloy 6061 chips after extrusion (500 °C).

Description	ET = 500 °C	ECAP-2	ECAP-4	ECAP-6
Relative density %	99.6	99.9	99.9	99.9
Microhardness, Vickers	41	94.5	103.5	110
Ultimate T. Strength, MPa	132.4	288.5	349	403
Grain size, μm	15.9	5	3.28	2.46

3. Results and Discussion

3.1. Process Operation Design

We shall consider the problem of designing the operation of cutting the aluminum workpiece as a hill-climbing problem in a vector space with Cartesian coordinates. In practice, the target function of this problem has several local minima in the feasibility region. There is certainly a need to find the global minimum or maximum in such studies.

The most promising method for solving these sorts of problems are dedicated search algorithms based on random strategies [58–60] and the projection of the informational bases of biological systems onto computing technologies. The most popular are currently ANN and genetic algorithms; both methods are effective in the field of local strategies and, most importantly, both provide the opportunity of exiting these fields during a global search.

Quality research requires a clear understanding of both the methodology and the research process. Experimental computer-based studies in the form of experimental simulations generally use multi-step methods. Graphical approaches to the target function surface used for this purpose build up graphical images and provide a reasonable representation of the computational experiment.

The mathematical procedure for system adaptation is essentially the investigation of a target function minimization problem in a certain convex area, D , of a normalized variable space, E . The target function is based on a convex numeric function or Q function that transposes area D onto a set of non-negative numbers. In the cutting tool-workpiece system adaptation problem, Q will determine the distance, r , between the point of convex area, D , and the origin of the coordinates of the normalized optimization criteria and the length of the vector, OR , in a non-negative multiobjective space E (Figure 4).

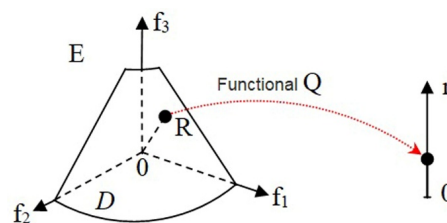


Figure 4. The Q function determines the distance between point R of a convex area, D , and the origin of coordinates of the normalized optimization criteria or the vector length, OR , in a non-negative multiobjective space, E .

Technical systems are steadily becoming more complex and the solutions to adaptation problem need complex setups for complicated control problems. Hence, modern adaptive systems must be complemented by artificial neural structures.

Firstly, the algorithm that calculates the optimum cutting parameters must be defined. A multicriterion optimization problem is initially set up, defining the criteria, the limitations, and the boundary conditions. The relationship is established between the machining parameters and the product parameters and the microstructure, employing a neural network to approximate the experimental data. A graphical interpretation of the surface of a normalized three-dimensional space is then created and the system states are determined, in which the values of each particular index cannot be improved without impairing the others, i.e., the Pareto frontier. In conclusion, the optimal workpiece turning conditions are defined that depend on both the physical and the mechanical properties of the alloy.

The following nomenclature is used: DM—decision maker; m —number of criteria; $I = \{1, 2, \dots, m\}$ —set of criterion numbers; X —set of possible decisions; $f = (f_1, f_2, \dots, f_m)$ —vector-valued criterion; $Y = f(X)$ —set of possible vectors (estimates); R_m —Euclidean space of m -dimensional vectors with real components; $>X$ —preference relation of DM specified in the set X ; $>Y$ —preference relation of DM, induced on the set with $>X$ and specified in the set Y ; $>$ —relation $>Y$ continued in the entire set R_m ; Sel X —set of selected decisions; Sel Y —set of selected vectors (estimates); Ndom X —set of non-dominated decisions; Ndom Y —set of non-dominated vectors (estimates); $Pf(X)$ —set of Pareto optimal decisions; $P(Y)$ —set of Pareto-optimal vectors (Pareto optimal estimates).

Graphically, the correlation of sets of vector estimates in a multiobjective environment is shown in Figure 5.

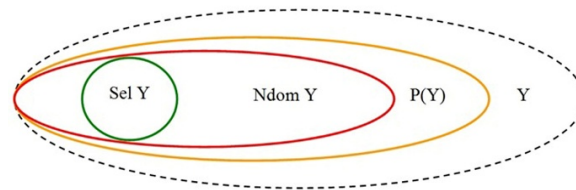


Figure 5. The relations of sets of vector estimates: the largest set is the set of possible estimates Y , and the smallest—a set of selected vectors, Sel Y .

3.2. Formulation of an Optimization Problem

The objective of the investigation of the machining operation implies the following optimization problem criteria: f_1 —surface roughness ($Ra, \mu\text{m}$) and f_2 —machining time for unit volume removal in one cutting tool pass ($T_m, \text{min}/\text{cm}^3$), and f_3 —the cost price of processing one part ($C, \$$), i.e., $m = 3$. Relatively, a set of possible Y estimates in the three-dimensional space, R^3 , is formed with vectors $f = (f_1, f_2, f_3)$. A search is then performed for a set of estimates having the minimum length of vector f , which is a vector from the origin of coordinates to a point on the estimate surface. Let us present the criteria in a normalized dimensionless form with the index 1 assigned to the maximum actual numbers.

The test system varied the parameters in accordance with the following experimental table (see Table 2): $x_1 = [100 \div 200]$ —cutting speed, v_c , m/min; $x_2 = [0.1 \div 0.4]$ —depth of cut, a_p , mm; $x_3 = [0.012 \div 0.15]$ —feed, f_r , mm/rev.

The state of the system was evaluated through four criteria (Tables 5–8). The first criterion was surface roughness, Ra (μm), or dimensionless surface roughness, $Ra^*(f_1)$; the second criterion was the unit volume machining time, T_m (min/cm^3), or the dimensionless unit volume machining time, $T_m^*(f_2)$. The third criterion was the cost price of processing one part, C (\$), or the dimensionless cost price of processing one part, $C^*(f_3)$. The fourth criterion was the dimensionless vector of estimates in a three-dimensional normalized space, f .

The values of the first criterion were taken from the experimental table and the rest were calculated on the basis of Formulas (3)–(8)

$$T_m = 1/(1000 \times v_c \times a_p \times f_r) \quad (3)$$

$$C_i = (C_{Mh} \times T^l) + (C_{Toolmin} \times T^l) + C_w, \quad (4)$$

where T_m is the machining time in turning, $T^l = (L + l_1)/(n \cdot f_r)$, where spindle speed $n = (1000 \cdot v_c)/(3.141 \cdot d)$; L is machining length section; l_1 is allowance length; d is diameter of cut.

$$Ra^* = Ra_i/Ra_{max}; \quad (5)$$

$$T_m^* = T_{m_i}/T_{m_{max}}; \quad (6)$$

$$C^* = C_i/C_{i_{max}}; \quad (7)$$

$$f = \sqrt{f_1^2 + f_2^2 + f_3^2} = \sqrt{Ra^{*2} + T_m^{*2} + C^{*2}} \quad (8)$$

where, Ra_i is surface roughness for the current combination of $X_{...}$ and f_r ; Ra_{max} is the maximum surface roughness value of all the v_c , a_p , and f_r combinations; T_{m_i} is the unit-volume machining time for the current values of v_c , a_p , and f_r ; $T_{m_{max}}$ is the maximum unit-volume machining time of all the v_c , a_p , and f_r combinations; C_i is the cost price of processing one part for the current combination of v_c , a_p , and f_r ; and $C_{i_{max}}$ is the maximum value.

The optimum search procedure involves a non-negative set of vector estimates and it eliminates the variation of parameter values below zero. The boundary condition is, therefore, that all the variables in this model are non-negative.

Now that the optimization problem is formulated, we shall build and train the four neural networks that should become the operators both for the functions of the three variables, $f(x_1, x_2, x_3)$ and $f(f_1, f_2, f_3)$, and for the Q functions on the planes, $f(f_1, f_2, f_3)$. The complex ANN was constructed using the Skif AURORA-SUSU supercomputer cluster (South Ural State University, Chelyabinsk, Russia).

Table 5. A selection of the optimization criteria parameter value set for the variable machining parameters of a workpiece hardened with ET-500.

Variable Parameters			Optimization Criteria							
x_1	x_2	x_3	Surface Roughness, Ra (μm)	Dimensionless Surface Roughness f_1 (Ra^*), u	Unit Volume Machining Time T_m (min/cm^3)	Dimensionless Unit Volume Machining Time of f_2 (T_m^*), u	The Cost Price of Processing One Part, C , (\$) Dimension-Less	Dimensionless Processing Cost Price of One Part f_3 (C^*), u	Vector Estimate Length f , u	Dimensionless Vector Estimate Length f^* , u
Cutting Speed, v_c , (m/min)	Depth of Cut, a_p (mm)	Feed, f_r , (mm/rev)								
100	0.2	0.012	0.159	0.066	4.167	0.5	7.640	0.37	0.673	0.469
150	0.2	0.012	0.161	0.067	2.778	0.333	7.425	0.36	0.555	0.387
200	0.2	0.012	0.170	0.071	2.083	0.25	7.320	0.355	0.509	0.355
100	0.2	0.045	0.302	0.126	1.111	0.133	7.170	0.347	0.514	0.358
150	0.2	0.045	0.305	0.127	0.741	0.089	7.113	0.345	0.504	0.351
200	0.2	0.045	0.320	0.133	0.556	0.067	7.085	0.343	0.505	0.352
100	0.2	0.081	0.399	0.166	0.617	0.074	7.094	0.344	0.538	0.375
150	0.2	0.081	0.405	0.168	0.412	0.049	7.063	0.342	0.536	0.374
150	0.2	0.081	0.408	0.169	0.412	0.049	7.063	0.342	0.537	0.374
150	0.2	0.081	0.410	0.17	0.412	0.049	7.063	0.342	0.538	0.375
150	0.2	0.081	0.405	0.168	0.412	0.049	7.063	0.342	0.536	0.374
200	0.2	0.081	0.417	0.173	0.309	0.037	7.048	0.341	0.539	0.376
100	0.2	0.15	1.989	0.826	0.333	0.04	7.052	0.342	0.972	0.677
150	0.2	0.15	1.998	0.83	0.222	0.027	7.033	0.341	0.973	0.678
200	0.2	0.15	2.000	0.831	0.167	0.02	7.026	0.34	0.973	0.678
100	0.25	0.012	0.241	0.1	3.333	0.4	7.640	0.37	0.630	0.439
150	0.25	0.012	0.251	0.104	2.222	0.267	7.425	0.36	0.552	0.385
200	0.25	0.012	0.241	0.1	1.667	0.2	7.320	0.355	0.516	0.360
100	0.25	0.045	0.248	0.103	0.889	0.107	7.170	0.347	0.485	0.338
150	0.25	0.045	0.271	0.113	0.593	0.071	7.113	0.345	0.487	0.339
200	0.25	0.045	0.294	0.122	0.444	0.053	7.085	0.343	0.492	0.343
100	0.25	0.081	0.287	0.119	0.494	0.059	7.094	0.344	0.491	0.342
150	0.25	0.081	0.356	0.148	0.329	0.039	7.063	0.342	0.516	0.360
150	0.25	0.081	0.349	0.145	0.329	0.039	7.063	0.342	0.513	0.357
150	0.25	0.081	0.352	0.146	0.329	0.039	7.063	0.342	0.514	0.358
150	0.25	0.081	0.350	0.145	0.329	0.039	7.063	0.342	0.513	0.357
200	0.25	0.081	0.446	0.185	0.247	0.03	7.048	0.341	0.550	0.383
100	0.25	0.15	1.976	0.821	0.267	0.032	7.052	0.342	0.969	0.675
150	0.25	0.15	1.868	0.776	0.178	0.021	7.033	0.341	0.945	0.659
200	0.25	0.15	2.240	0.931	0.133	0.016	7.026	0.34	1.023	0.713

Table 6. A selection of the optimization criteria parameter value set for the variable parameters of machining an ECAP-2 hardened workpiece.

Variable Parameters			Optimization Criteria							
x_1	x_2	x_3	Surface Roughness, Ra (μm)	Dimensionless Surface Roughness f_1 (Ra^*), u	Unit Volume Machining Time T_m (min/cm^3)	Dimensionless Unit Volume Machining Time of f_2 (T_m^*), u	The Cost Price of Processing One Part, C , (\$) Dimension-Less	Dimensionless Processing Cost Price of One Part f_3 (C^*), u	Vector Estimate Length f , u	Dimensionless Vector Estimate Length f^* , u
Cutting Speed, v_c , (m/min)	Depth of Cut, a_p , (mm)	Feed, f_r , (mm/rev)								
100	0.2	0.012	0.235	0.098	4.167	0.5	12.640	0.612	0.850	0.592
150	0.2	0.012	0.242	0.101	2.778	0.333	12.425	0.602	0.758	0.528
200	0.2	0.012	0.249	0.103	2.083	0.25	12.320	0.597	0.722	0.503
100	0.2	0.045	0.258	0.107	1.111	0.133	12.170	0.59	0.688	0.479
150	0.2	0.045	0.264	0.11	0.741	0.089	12.113	0.587	0.680	0.474
200	0.2	0.045	0.271	0.113	0.556	0.067	12.085	0.586	0.679	0.473
100	0.2	0.081	0.361	0.15	0.617	0.074	12.094	0.586	0.706	0.492
150	0.2	0.081	0.370	0.154	0.412	0.049	12.063	0.584	0.705	0.491
150	0.2	0.081	0.372	0.154	0.412	0.049	12.063	0.584	0.705	0.491
150	0.2	0.081	0.370	0.154	0.412	0.049	12.063	0.584	0.705	0.491
150	0.2	0.081	0.370	0.154	0.412	0.049	12.063	0.584	0.705	0.491
200	0.2	0.081	0.381	0.158	0.309	0.037	12.048	0.584	0.707	0.493
100	0.2	0.15	1.812	0.753	0.333	0.04	12.052	0.584	1.047	0.730
150	0.2	0.15	1.819	0.756	0.222	0.027	12.033	0.583	1.047	0.730
200	0.2	0.15	1.826	0.758	0.167	0.02	12.026	0.583	1.048	0.730
100	0.25	0.012	0.217	0.09	3.333	0.4	12.640	0.612	0.790	0.551
150	0.25	0.012	0.226	0.094	2.222	0.267	12.425	0.602	0.726	0.506
200	0.25	0.012	0.232	0.096	1.667	0.2	12.320	0.597	0.702	0.489
100	0.25	0.045	0.192	0.08	0.889	0.107	12.170	0.59	0.663	0.462
150	0.25	0.045	0.220	0.091	0.593	0.071	12.113	0.587	0.664	0.463
200	0.25	0.045	0.226	0.094	0.444	0.053	12.085	0.586	0.663	0.462
100	0.25	0.081	0.309	0.128	0.494	0.059	12.094	0.586	0.689	0.480
150	0.25	0.081	0.320	0.133	0.329	0.039	12.063	0.584	0.690	0.481
150	0.25	0.081	0.318	0.132	0.329	0.039	12.063	0.584	0.689	0.480
150	0.25	0.081	0.317	0.132	0.329	0.039	12.063	0.584	0.689	0.480
150	0.25	0.081	0.315	0.131	0.329	0.039	12.063	0.584	0.688	0.479
200	0.25	0.081	0.343	0.142	0.247	0.03	12.048	0.584	0.696	0.485
100	0.25	0.15	1.778	0.739	0.267	0.032	12.052	0.584	1.040	0.725
150	0.25	0.15	1.729	0.718	0.178	0.021	12.033	0.583	1.029	0.717
200	0.25	0.15	2.016	0.838	0.133	0.016	12.026	0.583	1.085	0.756

Table 7. A selection of the optimization criteria parameter value set for the variable machining parameters of a workpiece hardened with ECAP-4.

Variable Parameters			Optimization Criteria							
x_1	x_2	x_3	Surface Roughness, Ra (μm)	Dimensionless Surface Roughness f_1 (Ra^*), u	Unit Volume Machining Time T_m (min/cm^3)	Dimensionless Unit Volume Machining Time of f_2 (T_m^*), u	The Cost Price of Processing One Part, C , (\$) Dimension-Less	Dimensionless Processing Cost Price of One Part f_3 (C^*), u	Vector Estimate Length f , u	Dimensionless Vector Estimate Length f^* , u
Cutting Speed, v_c , (m/min)	Depth of Cut, a_p , (mm)	Feed, f_r , (mm/rev)								
100	0.2	0.012	0.226	0.094	4.167	0.5	16.640	0.806	0.997	0.695
150	0.2	0.012	0.240	0.1	2.778	0.333	16.425	0.796	0.919	0.640
200	0.2	0.012	0.253	0.105	2.083	0.25	16.320	0.791	0.891	0.621
100	0.2	0.045	0.273	0.114	1.111	0.133	16.170	0.783	0.863	0.601
150	0.2	0.045	0.284	0.118	0.741	0.089	16.113	0.781	0.858	0.598
200	0.2	0.045	0.296	0.123	0.556	0.067	16.085	0.779	0.857	0.597
100	0.2	0.081	0.354	0.147	0.617	0.074	16.094	0.78	0.872	0.608
150	0.2	0.081	0.370	0.154	0.412	0.049	16.063	0.778	0.873	0.608
150	0.2	0.081	0.367	0.153	0.412	0.049	16.063	0.778	0.872	0.608
150	0.2	0.081	0.367	0.153	0.412	0.049	16.063	0.778	0.872	0.608
200	0.2	0.081	0.381	0.158	0.309	0.037	16.048	0.778	0.874	0.609
100	0.2	0.15	1.749	0.727	0.333	0.04	16.052	0.778	1.155	0.805
150	0.2	0.15	1.763	0.732	0.222	0.027	16.033	0.777	1.156	0.806
200	0.2	0.15	1.776	0.738	0.167	0.02	16.026	0.776	1.158	0.807
100	0.25	0.012	0.213	0.088	3.333	0.4	16.640	0.806	0.947	0.660
150	0.25	0.012	0.222	0.092	2.222	0.267	16.425	0.796	0.893	0.622
200	0.25	0.012	0.228	0.095	1.667	0.2	16.320	0.791	0.872	0.608
100	0.25	0.045	0.228	0.095	0.889	0.107	16.170	0.783	0.848	0.591
150	0.25	0.045	0.237	0.098	0.593	0.071	16.113	0.781	0.844	0.588
200	0.25	0.045	0.257	0.107	0.444	0.053	16.085	0.779	0.847	0.590
100	0.25	0.081	0.352	0.146	0.494	0.059	16.094	0.78	0.871	0.607
150	0.25	0.081	0.314	0.13	0.329	0.039	16.063	0.778	0.858	0.598
150	0.25	0.081	0.311	0.129	0.329	0.039	16.063	0.778	0.858	0.598
150	0.25	0.081	0.310	0.129	0.329	0.039	16.063	0.778	0.858	0.598
150	0.25	0.081	0.309	0.128	0.329	0.039	16.063	0.778	0.857	0.597
200	0.25	0.081	0.372	0.155	0.247	0.03	16.048	0.778	0.872	0.608
100	0.25	0.15	1.743	0.724	0.267	0.032	16.052	0.778	1.153	0.803
150	0.25	0.15	1.629	0.677	0.178	0.021	16.033	0.777	1.132	0.789
200	0.25	0.15	1.976	0.821	0.133	0.016	16.026	0.776	1.193	0.831

Table 8. A selection of the optimization criteria parameter value set for the variable parameters of machining of a workpiece hardened with ECAP-6.

Variable Parameters			Optimization Criteria							
x_1	x_2	x_3	Surface Roughness, Ra (μm)	Dimensionless Surface Roughness f_1 (Ra^*), u	Unit Volume Machining Time T_m (min/cm^3)	Dimensionless Unit Volume Machining Time of f_2 (T_m^*), u	The Cost Price of Processing One Part, C , (\$) Dimension-Less	Dimensionless Processing Cost Price of One Part f_3 (C^*), u	Vector Estimate Length f , u	Dimensionless Vector Estimate Length f^* , u
Cutting Speed, v_c , (m/min)	Depth of Cut, a_p , (mm)	Feed, f_r , (mm/rev)								
100	0.2	0.012	0.470	0.195	4.167	0.5	20.640	1	1.202	0.838
150	0.2	0.012	0.672	0.279	2.778	0.333	20.425	0.99	1.170	0.815
200	0.2	0.012	0.874	0.363	2.083	0.25	20.320	0.984	1.181	0.823
100	0.2	0.045	0.262	0.109	1.111	0.133	20.170	0.977	1.040	0.725
150	0.2	0.045	0.276	0.114	0.741	0.089	20.113	0.974	1.035	0.721
200	0.2	0.045	0.289	0.12	0.556	0.067	20.085	0.973	1.035	0.721
100	0.2	0.081	0.334	0.139	0.617	0.074	20.094	0.974	1.046	0.729
150	0.2	0.081	0.358	0.149	0.412	0.049	20.063	0.972	1.047	0.730
150	0.2	0.081	0.352	0.146	0.412	0.049	20.063	0.972	1.046	0.729
150	0.2	0.081	0.354	0.147	0.412	0.049	20.063	0.972	1.046	0.729
150	0.2	0.081	0.352	0.146	0.412	0.049	20.063	0.972	1.046	0.729
200	0.2	0.081	0.363	0.151	0.309	0.037	20.048	0.971	1.047	0.730
100	0.2	0.15	1.781	0.74	0.333	0.04	20.052	0.972	1.299	0.905
150	0.2	0.15	1.796	0.746	0.222	0.027	20.033	0.971	1.300	0.906
200	0.2	0.15	1.814	0.754	0.167	0.02	20.026	0.97	1.302	0.907
100	0.25	0.012	0.209	0.087	3.333	0.4	20.640	1	1.117	0.778
150	0.25	0.012	2.173	0.903	2.222	0.267	20.425	0.99	1.398	0.974
200	0.25	0.012	0.224	0.093	1.667	0.2	20.320	0.984	1.049	0.731
100	0.25	0.045	0.222	0.092	0.889	0.107	20.170	0.977	1.029	0.717
150	0.25	0.045	0.224	0.093	0.593	0.071	20.113	0.974	1.023	0.713
200	0.25	0.045	0.242	0.101	0.444	0.053	20.085	0.973	1.025	0.714
100	0.25	0.081	0.291	0.121	0.494	0.059	20.094	0.974	1.036	0.722
150	0.25	0.081	0.309	0.128	0.329	0.039	20.063	0.972	1.036	0.722
150	0.25	0.081	0.305	0.127	0.329	0.039	20.063	0.972	1.036	0.722
150	0.25	0.081	0.306	0.127	0.329	0.039	20.063	0.972	1.036	0.722
150	0.25	0.081	0.304	0.126	0.329	0.039	20.063	0.972	1.036	0.722
200	0.25	0.081	0.327	0.136	0.247	0.03	20.048	0.971	1.039	0.724
100	0.25	0.15	1.717	0.713	0.267	0.032	20.052	0.972	1.288	0.898
150	0.25	0.15	1.839	0.764	0.178	0.021	20.033	0.971	1.307	0.911
200	0.25	0.15	1.946	0.809	0.133	0.016	20.026	0.97	1.323	0.922

3.3. Building a Neural Network

Matlab is a leading software package, from among other mathematical software—Maple, Mathematica and Mathcad—designed for versatile numeric calculations of fundamental quality. The Neural Network Toolbox in Matlab, designed to create models and to train them, facilitates neural network creation. An undeniable advantage of Matlab is its language, with which users can create their own algorithms and applications. The versatility of the language provides opportunities for accomplishing a number of tasks such as collecting, analyzing, and structuring data, developing algorithms, modeling systems, object-oriented programming, development of a graphical user interface, debugging and converting Matlab applications to C or C++ code. Hence, the programming environment of choice, which is Matlab R2010b (parallel processing version).

The controlled feedforward neural network in the form of a multilayer perceptron (MLP) was trained with the Levenberg–Marquardt algorithm. The network structure was embedded in a hidden layer of sigmoid neurons and a linear layer of output neurons, which is the best structure for multidimensional mapping problems.

Only the normalized values with respect to the maximum were used for training the network. They were limited to the [0.1] range that improved the efficiency of the training.

Improvements to the generalization performance of the network solved the overfitting problem. Two data sets were used to do so: the training set that updated weights and offsets, and the validation set that stops the training when an undesirable event occurs.

The final configuration (the number of neurons in the hidden layer) of the network will be established based on the lowest mean squared error of the validation set.

The multilayer perceptrons were, to begin with, trained with nine, 10, and 11 neurons in the hidden layer, with 15% of the tabular data allocated to the validation set. Having done the calculations for each of the hardening methods (ET500, ECAP-2, ECAP-4, ECAP-6), the lowest error values for MLP 3-10-4, presented in Figure 6a–d were computed.

The coefficients of determination (R^2) with respect to criterion f were 0.992 for the ET500 hardening method, $R^2 = 0.956$ for the ECAP-2 hardening method, $R^2 = 0.988$ for the ECAP-4 hardening method, and $R^2 = 0.991$ for the ECAP-6 hardening method, which reflects the high accuracy of the neural network prediction model $\pm 0.8\%$, $\pm 4.4\%$, $\pm 1.9\%$ and $\pm 1.1\%$, respectively. The same structure appeared to be the best in generalization performance when 10% or 20% were allocated in the validation set of tabular data, shown in Figure 6d. In the case of allocating 10% of the training set, the mean square errors of the networks were 0.0021 for the ET500 hardening method; 0.0032 for the ECAP-2 hardening method; 0.0022 for the ECAP-4 hardening method; 0.0045 for the ECAP-6 hardening method, and in the case of allocating 15% the mean square errors of the networks were 0.0018 for the ET500 hardening method; 0.0028 for the ECAP-2 hardening method; 0.0019 for the ECAP-4 hardening method; and 0.0031 for the ECAP-6 hardening method, respectively.

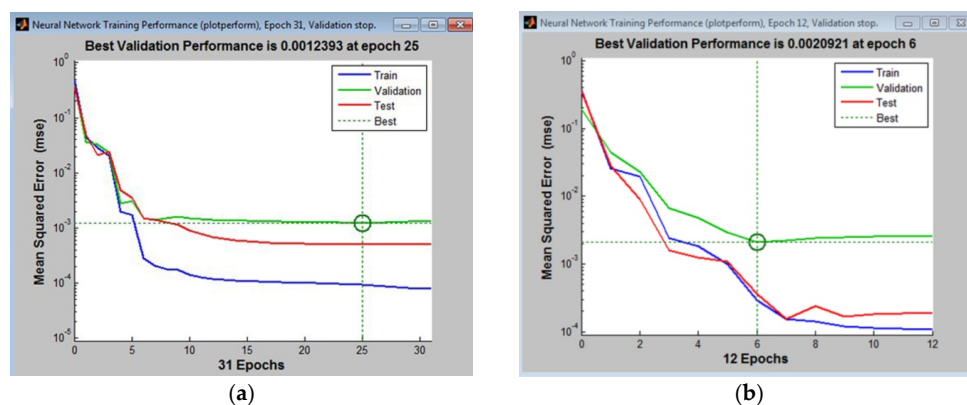


Figure 6. Cont.

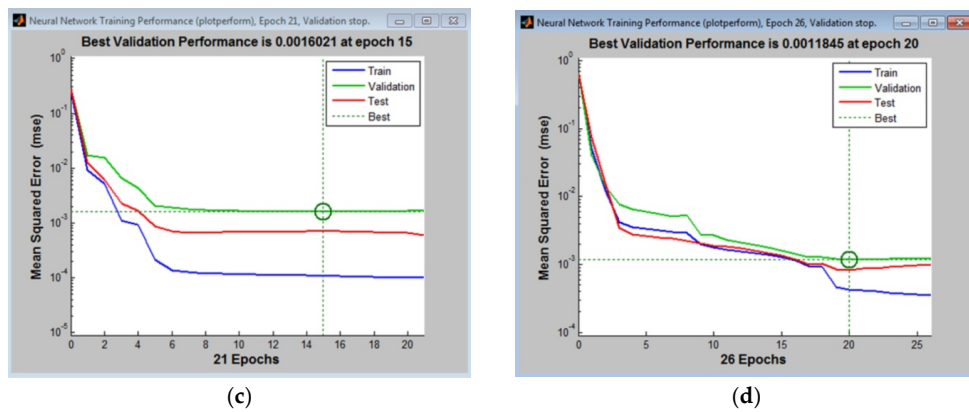


Figure 6. The lowest mean squared error (LMSE) for the validation set in MLP 3-10-4 and the (a) ET500; ECAP-2 (b); ECAP-4 (c); ECAP-6 (d) hardening method configuration (calculated in Matlab).

3.4. Graphical Representation of the Surface of Vector Estimates *d*

The MLP 3-10-4 model and the experimental values of x_1, x_2 and x_3 were used to calculate f_1, f_2 and f_3 , to build the surface of vector estimates, *D*.

The non-linear surfaces, *D*, were projected (3D wafer plots of Ra^* values) onto the plane $f_2 f_3$ ($C^* T_m^*$) for the four methods of hardening the aluminum workpiece, Figure 7a–d.

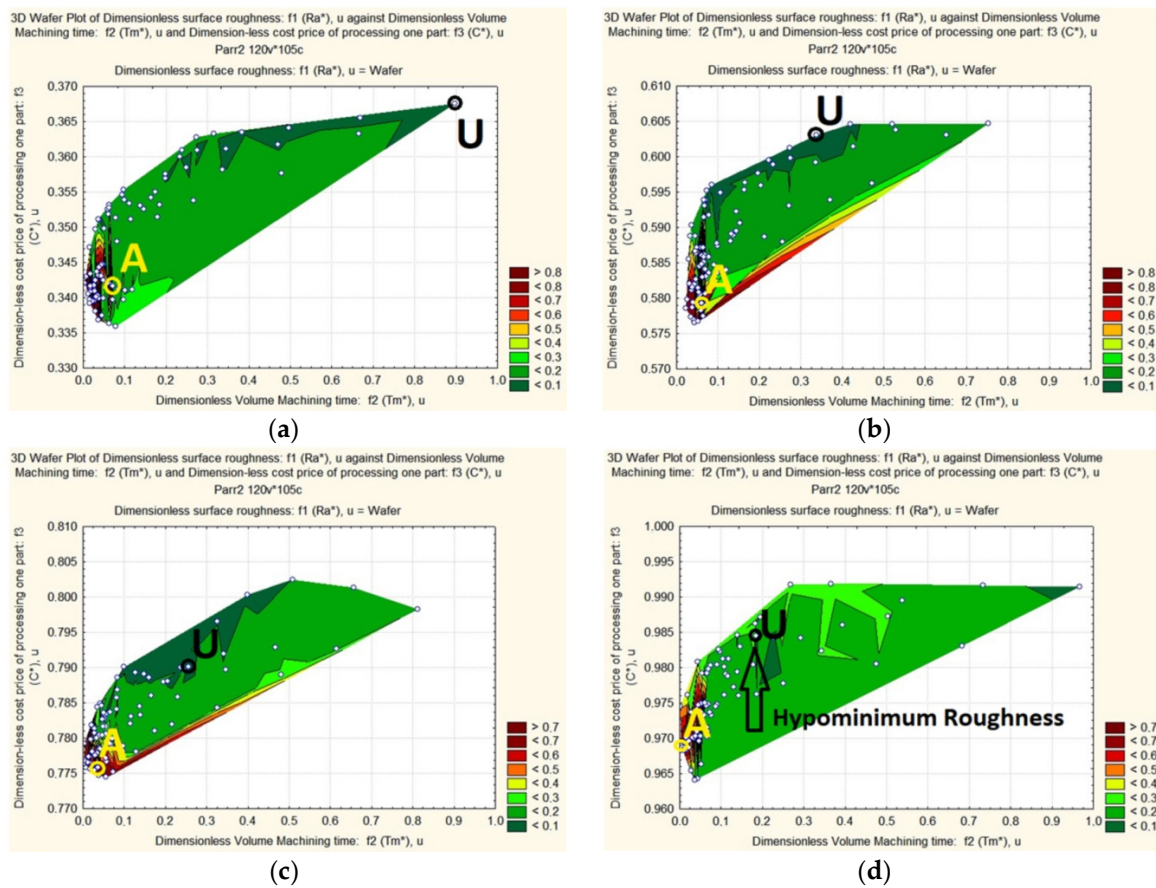


Figure 7. 3D wafer plot of Ra^* values for the machined workpiece with respect to changes in C^* and T_m^* values ((a) method of obtaining an AA6061 alloy workpiece with ET-500 extrusion); (b) ECAP-2; (c) ECAP-4; (d) ECAP-6 hardening of an AA6061 workpiece.

The following paragraphs set out an analysis of the Ra^* wafer plots.

On the plots (see Figure 7a–d), we can clearly see apexes A in the area of minimal values C^* and T_m^* and the slopes and dents of U. When the coordinates of these points are determined, for an extruded AA6061 alloy workpiece the following points were obtained: points A (0.876; 0.063; 0.342; 0.706) and U (0.068; 0.897; 0.368; 0.668) for ET-500 extrusion; points A (0.842; 0.069; 0.579; 0.761) and U (0.084; 0.339; 0.603; 0.536) for ECAP-2 workpiece hardening; points A (0.767; 0.016; 0.777; 0.818) and U (0.081; 0.257; 0.790; 0.628) for ECAP-4 workpiece hardening; and points A (0.793; 0.004; 0.969; 0.913) and U (0.061; 0.185; 0.985; 0.737) for ECAP-6 workpiece hardening.

On the plots, the changes of the last two criteria are within certain limits. In the case of obtaining an AA6061 alloy workpiece by ET-500 extrusion (see Figure 7a), T_m^* changed from 0.010 to 0.900 units, and $C^* = 0.336$ to 0.368 units. In the case of ECAP-2 workpiece hardening, T_m^* (see Figure 7b) changed from 0.250 to 0.760, and $C^* = 0.577$ to 0.604 units. In the case of ECAP-4 hardening of the workpiece (see Figure 7c), T_m^* changed from 0.010 to 0.810, and $C^* = 0.774$ to 0.802 units. In the case of ECAP-6 hardening of the workpiece, T_m^* (see Figure 7d) changed from 0.010 to 0.960, and $C^* = 0.964$ to 0.992 units.

The conclusion is that the refinement of both the structure and the properties of an AA6061 alloy workpiece following ECAP hardening results in displacement of the optimization criteria limits: the minimum value of Ra^* decreased by 76%, and the maximum value by 8%; the minimum value of T_m^* stayed unchanged, the maximum—increased by 6%; the minimum value of C^* increased 2.8-fold, and the maximum increased 3-fold. Hyperminimum surface roughness was attained in the case of ECAP-6 hardening of the workpiece (p. U in Figure 8d).

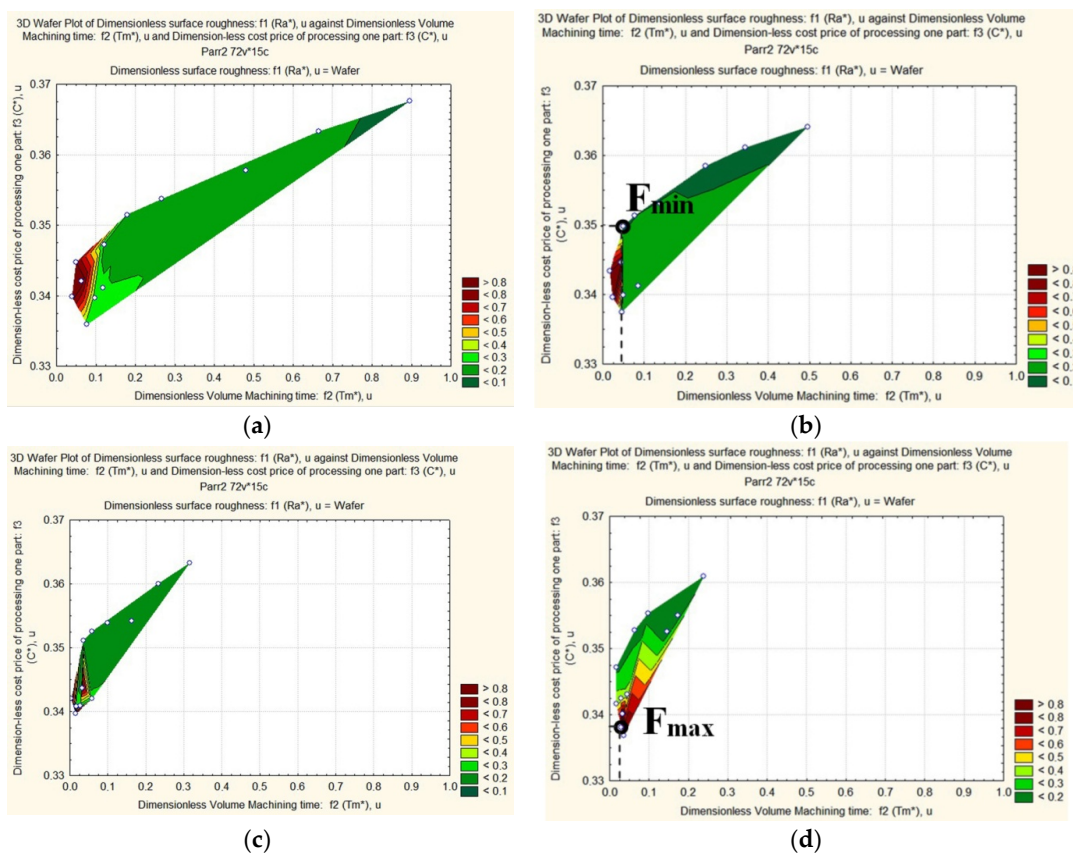


Figure 8. Surface projections of Ra^* values depending on the change in the values of C^* and T_m^* at a fixed depth of cut (the case of obtaining an AA6061 alloy workpiece with ET-500 extrusion): (a) $a_p = 0.1$ mm; (b) $a_p = 0.2$ mm; (c) $a_p = 0.3$ mm; (d) $a_p = 0.4$ mm.

3.5. Establishment of a Pareto Frontier

The target function is represented by a vector length in a normalized space that connects the origin of the coordinates with the point of the three-dimensional surface of estimates. The shortest length at the foot of the apexes, A , of the Ra^* ridge, in the area with the lowest C^* and T_m^* values, have to be defined (see Figure 7a–d). For this purpose, we shall consider projections of surface estimates at fixed depths of cut: $a_p = 0.1$ mm, $a_p = 0.15$ mm, $a_p = 0.2$ mm, $a_p = 0.25$ mm, $a_p = 0.3$ mm, $a_p = 0.35$ mm, and $a_p = 0.4$ mm (Figures 8–11).

The above figures (Figures 8–11) depict a decreasing depth of cut from $a_p = 0.1$ to $a_p = 0.4$ mm, while the area of the maximum values of dimensionless roughness transforms itself into a decreased projection area due to its shorter ridges. The surface roughness projection area also decreased: in the case of ET-500, the area decreased 1.75-fold (see Figure 8a–d), in the case of ECAP-2 hardening, the area decreased 1.81-fold (see Figure 9a–d), in the case of ECAP-4, the area decreased 2.45-fold (see Figure 10a–d), and in the case of ECAP-6, the area decreased 3.1-fold (see Figure 11a–d).

Considering the data on changes in structure and characteristics of alloy AA6061 (see Table 2) and having compared the cutting conditions (see Tables 5–8) with the surface roughness wafer plots (see Figures 8–11), the effect may be explained as follows.

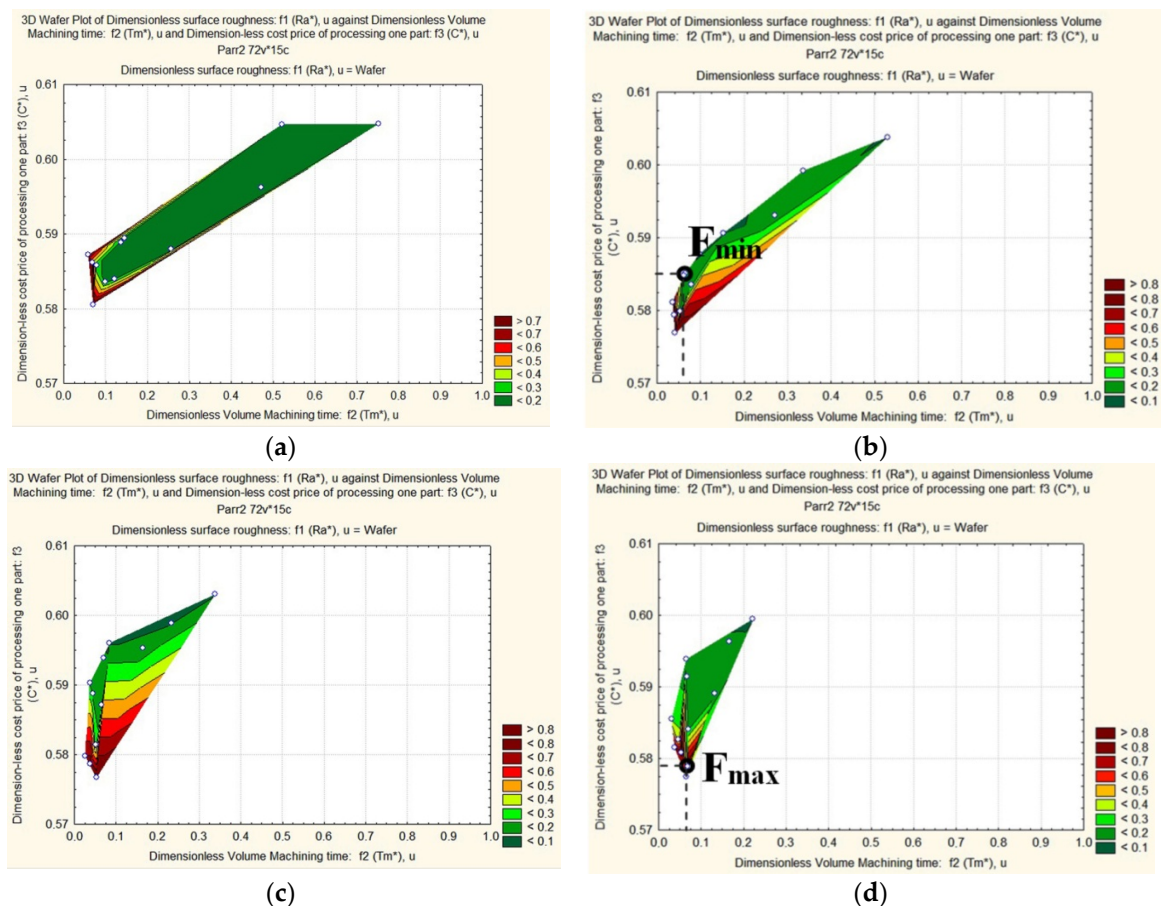


Figure 9. Surface projections of Ra^* values depending on the change in the values of C^* and T_m^* at a fixed depth of cut (ECAP-2 hardening of an AA6061 alloy workpiece): (a) $a_p = 0.1$ mm; (b) $a_p = 0.2$ mm; (c) $a_p = 0.3$ mm; (d) $a_p = 0.4$ mm.

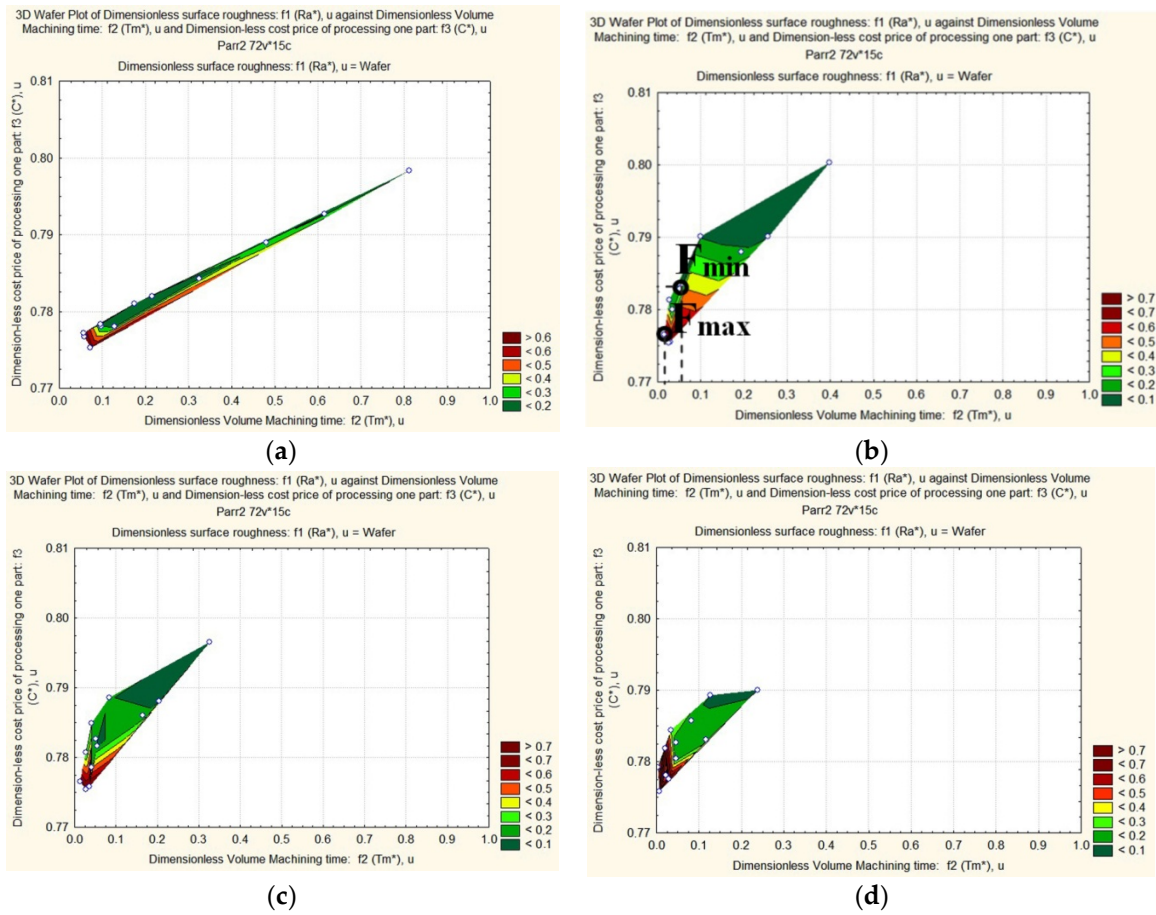


Figure 10. Surface projections of Ra^* values depending on the change in the values of C^* and T_m^* at a fixed depth of cut (ECAP-4 hardening of an AA6061 alloy workpiece): (a) $a_p = 0.1$ mm; (b) $a_p = 0.25$ mm; (c) $a_p = 0.3$ mm; (d) $a_p = 0.4$ mm.

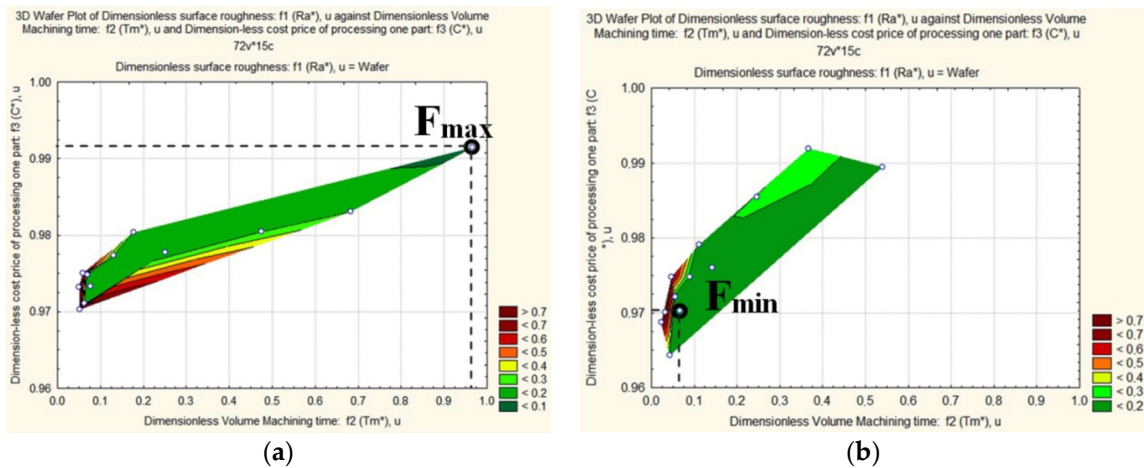


Figure 11. Cont.

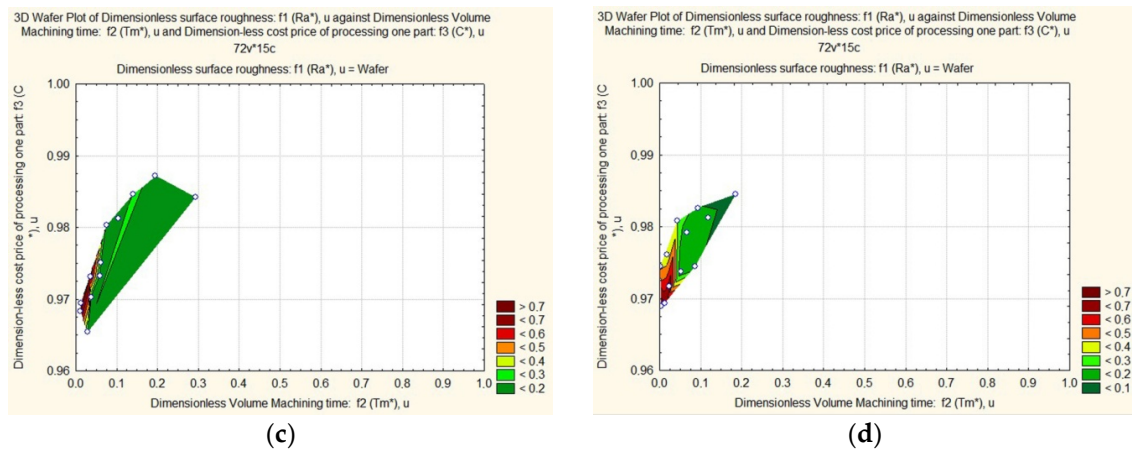


Figure 11. Surface projections of Ra^* values depending on the change in the values of C^* and T_m^* at a fixed depth of cut (ECAP-6 hardening of an AA6061 alloy workpiece): (a) $a_p = 0.1$ mm; (b) $a_p = 0.2$ mm; (c) $a_p = 0.3$ mm; (d) $a_p = 0.4$ mm.

The chip samples extruded at $500\text{ }^\circ\text{C}$ had a grain size of $15.9\text{ }\mu\text{m}$ and the effect of 2, 4, and 6 ECAP passes resulted in grain refinement of about 5, 3.28 and $2.46\text{ }\mu\text{m}$ respectively. Grain refinement was accompanied by an increase in microhardness hardness from 41 HV to 110 HV and an increase in the ultimate tensile strength from 132.4 to 403 MPa, as shown in Table 4. The higher hardness consequently resulted in improved surface finish; due to the hardness of the processed material and low plastic flow capability. A behavior that was attributed to the brittle nature of the interaction between the cutting tool and the workpiece surface, in the same way as in hard materials, which provoked material separation rather than plastic flow that resulted in surface irregularities. Surface roughness was found to increase at increasing feed rates and depths of cut, which resulted in larger cut areas that were consequently associated with higher cutting forces and higher friction. These values, once again, resulted in a poor surface finish. It was noted from the surface roughness profile that high feed rates were associated with higher roughness levels marking horizontal spacing. At higher depth of cuts, the vertical spacing between peaks and valleys of the surface irregularities was also larger. Thus, higher feed rates and depth of cuts led to higher surface roughness (see Tables 5–8).

T_m^* was the design criterion and its value was only determined by the cutting conditions (v_c , a_p , f_r). It was not dependent on the properties of the machined material (see Formula (1)). Hence, the range of this criterion in no way depended on the hardening method selected for the AA6061 alloy.

Having analyzed the representation of the second criterion C^* (see Formula (2)), it was concluded that the major contribution to the cost of machining was due to the AA6061 alloy hardening process. The range of C^* values tripled when ECAP-6 was chosen, in which case the maximum strength (microhardness and limit strength) of AA6061 and the minimum surface roughness were obtained.

The optimum has to be located at the foot of the apexes, A, in the area of high-speed turning conditions at which maximum tool wear is possible. According to Figures 8–11, the cutting conditions are limited to a depth of cut of $a_p = 0.2$ mm (obtaining an AA6061 workpiece with ET-500 extrusion), f (0.096; 0.050; 0.350; 0.134), $a_p = 0.2$ mm; (ECAP-2 hardening of an AA6061 alloy workpiece f (0.112; 0.065; 0.585; 0.462), $a_p = 0.25$ mm; (ECAP-4 hardening of an AA6061 alloy workpiece, f (0.083; 0.055; 0.783; 0.582), and $a_p = 0.2$ mm; and (ECAP-6 hardening of an AA6061 alloy workpiece, f (0.115; 0.066; 0.970; 0.715), because in this case all the Ra^* values were located near the minimum vector estimation, f , which are marked by the points F_{min} . The maximum vector estimates, f , are marked by the F_{max} points.

At these depths of cut and F_{min} , three graphical dependencies, $Ra^* = f(C^*, T_m^*)$, were constructed. Each one corresponded to the fixed $v_c = 100$ m/min, $v_c = 150$ m/min, $v_c = 200$ m/min and variable f_r . After matching the curves with the projections (see Figures 8b, 9b, 10b and 11b), we obtained reference points for the Pareto frontier. The following cases are shown in Figure 12a–d: an AA6061 workpiece

obtained with ET-500 extrusion p_1 (0.857; 0.024; 0.340); p_2 (0.182; 0.046; 0.337); p_3 (0.157; 0.050; 0.340); p_4 (0.096; 0.050; 0.350); p_5 (0.098; 0.078; 0.351); p_6 (0.075; 0.249; 0.358); p_7 (0.069; 0.345; 0.361); p_8 (0.078; 0.496; 0.364) (see Figure 12a); ECAP-2 hardening of an AA6061 alloy workpiece p_1 (0.804; 0.042; 0.577); p_2 (0.170; 0.054; 0.580); p_3 (0.112; 0.065; 0.585); p_4 (0.094; 0.098; 0.588); p_5 (0.097; 0.153; 0.591); p_6 (0.107; 0.337; 0.599); p_7 (0.099; 0.530; 0.604) (see Figure 12b); ECAP-4 hardening of an AA6061 alloy workpiece p_1 (0.767; 0.016; 0.777); p_2 (0.736; 0.026; 0.775); p_3 (0.708; 0.029; 0.776); p_4 (0.147; 0.034; 0.780); p_5 (0.083; 0.055; 0.783); p_6 (0.092; 0.100; 0.790); p_7 (0.091; 0.398; 0.800) (see Figure 12c) and ECAP-6 hardening of an AA6061 alloy workpiece p_1 (0.758; 0.032; 0.970); p_2 (0.165; 0.043; 0.964); p_3 (0.115; 0.066; 0.970); p_4 (0.104; 0.143; 0.976); p_5 (0.149; 0.539; 0.989) (see Figure 12d).

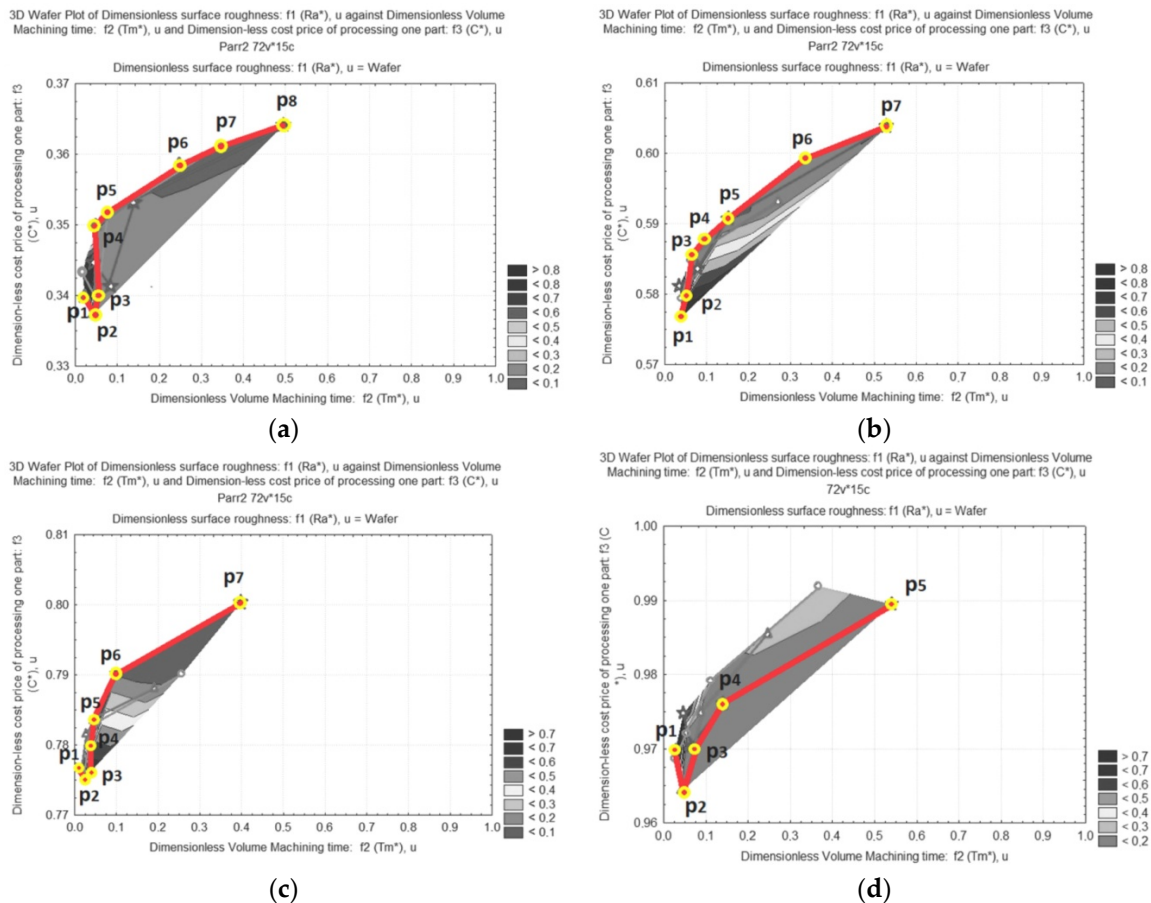


Figure 12. The Pareto frontier and eight reference points in the case of: (a) obtaining an AA6061 workpiece with ET-500 extrusion: p_1 (0.857; 0.024; 0.340); p_2 (0.182; 0.046; 0.337); p_3 (0.157; 0.050; 0.340); p_4 (0.096; 0.050; 0.350); p_5 (0.098; 0.078; 0.351); p_6 (0.075; 0.249; 0.358); p_7 (0.069; 0.345; 0.361); p_8 (0.078; 0.496; 0.364); (b) ECAP-2 hardening of an AA6061 alloy workpiece: p_1 (0.804; 0.042; 0.577); p_2 (0.170; 0.054; 0.580); p_3 (0.112; 0.065; 0.585); p_4 (0.094; 0.098; 0.588); p_5 (0.097; 0.153; 0.591); p_6 (0.107; 0.337; 0.599); p_7 (0.099; 0.530; 0.604); (c) ECAP-4 hardening of an AA6061 alloy workpiece: p_1 (0.767; 0.016; 0.777); p_2 (0.736; 0.026; 0.775); p_3 (0.708; 0.029; 0.776); p_4 (0.147; 0.034; 0.780); p_5 (0.083; 0.055; 0.783); p_6 (0.092; 0.100; 0.790); p_7 (0.091; 0.398; 0.800); (d) ECAP-6 hardening of an AA6061 alloy workpiece: p_1 (0.758; 0.032; 0.970); p_2 (0.165; 0.043; 0.964); p_3 (0.115; 0.066; 0.970); p_4 (0.104; 0.143; 0.976); p_5 (0.149; 0.539; 0.989).

The Pareto frontier for the aluminum workpiece obtained with ET-500 extrusion (see Figure 12a) has the following sections. Section I, between point p_1 and point p_2 , corresponds to the following cutting conditions: $v_c = 200$ m/min, $a_p = 0.20$ mm, $f_r = 0.15 \dots 0.081$ mm/rev. Section II, between point p_2 and point p_3 , corresponds to the following cutting conditions: $v_c = 200 \dots 150$ m/min,

$a_p = 0.20$ mm, $f_r = 0.081$ mm/rev. Section III, between point p_3 and point p_4 , corresponds to the following cutting conditions: $v_c = 150 \dots 200$ m/min, $a_p = 0.20$ mm, $f_r = 0.081 \dots 0.045$ mm/rev. Section IV, between points p_4 and p_5 , corresponds to the following cutting conditions: $v_c = 200 \dots 150$ m/min, $a_p = 0.20$ mm, $f_r = 0.045$ mm/rev. Section V, between points p_5 and p_6 , corresponds to the following cutting conditions: $v_c = 150 \dots 200$ m/min, $a_p = 0.20$ mm, $f_r = 0.45 \dots 0.012$ mm/rev. Section VI, between points p_6 and p_7 , corresponds to the following cutting conditions: $v_c = 200 \dots 150$ m/min, $a_p = 0.20$ mm, $f_r = 0.012$ mm/rev. Section VII, between points p_7 and p_8 , corresponds to the following cutting conditions: $v_c = 150 \dots 100$ m/min, $a_p = 0.20$ mm, $f_r = 0.012$ mm/rev. p_3 is a special point on the Pareto curve. These points correspond to absolute minimums of the length of vector f^* ($Ra^* = 0.096$ u, $T_m^* = 0.050$ u, $C^* = 0.350$ u, $f^* = 0.314$ u).

The Pareto frontier for the ECAP-2 hardened aluminum workpiece (see Figure 12b) has the following sections. Section I, between point p_1 and point p_2 corresponds to the following cutting conditions: $v_c = 200$ m/min, $a_p = 0.20$ mm, $f_r = 0.15 \dots 0.081$ mm/rev. Section II, between point p_2 and point p_3 , corresponds to the following cutting conditions: $v_c = 200$ m/min, $a_p = 0.20$ mm, $f_r = 0.081 \dots 0.045$ mm/rev. Section III, between point p_3 and point p_4 , corresponds to the following cutting conditions: $v_c = 200 \dots 150$ m/min, $a_p = 0.20$ mm, $f_r = 0.045$ mm/rev. Section IV, between points p_4 and p_5 , corresponds to the following cutting conditions: $v_c = 150 \dots 100$ m/min, $a_p = 0.20$ mm, $f_r = 0.045$ mm/rev. Section V, between points p_5 and p_6 , corresponds to the following cutting conditions: $v_c = 100 \dots 150$ m/min, $a_p = 0.50$ mm, $f_r = 0.045 \dots 0.012$ mm/rev. Section VI, between points p_6 and p_7 , corresponds to the following cutting conditions: $v_c = 150 \dots 100$ m/min, $a_p = 0.20$ mm, $f_r = 0.012$ mm/rev. p_3 is a special point on the Pareto curve. These points correspond to the absolute minimum of the length of vector f^* ($Ra^* = 0.112$ u, $T_m^* = 0.065$ u, $C^* = 0.585$ u, $f^* = 0.462$ u).

The Pareto frontier for the ECAP-4 hardened aluminum workpiece (see Figure 12c) has the following sections. Section I, between point p_1 and point p_2 , corresponds to the following cutting conditions: $v_c = 200 \dots 150$ m/min, $a_p = 0.25$ mm, $f_r = 0.15$ mm/rev. Section II, between point p_2 and point p_3 , corresponds to the following cutting conditions: $v_c = 150 \dots 100$ m/min, $a_p = 0.25$ mm, $f_r = 0.15$ mm/rev. Section III, between point p_3 and point p_4 , corresponds to the following cutting conditions: $v_c = 100 \dots 150$ m/min, $a_p = 0.25$ mm, $f_r = 0.15 \dots 0.081$ mm/rev. Section IV, between points p_4 and p_5 , corresponds to the following cutting conditions: $v_c = 150$ m/min, $a_p = 0.25$ mm, $f_r = 0.081 \dots 0.045$ mm/rev. Section V, between points p_5 and p_6 , corresponds to the following cutting conditions: $v_c = 150 \dots 100$ m/min, $a_p = 0.25$ mm, $f_r = 0.045$ mm/rev. Section VI, between points p_6 and p_7 , corresponds to the following cutting conditions: $v_c = 100$ m/min, $a_p = 0.25$ mm, $f_r = 0.045 \dots 0.012$ mm/rev. p_1 and p_5 are special points on the Pareto curve. p_1 is the absolute maximum of surface roughness Ra^* ($Ra^* = 0.767$ u, $T_m^* = 0.016$ u, $C^* = 0.777$ u, $f^* = 0.818$ u). p_5 is the absolute minimum of the length of vector f^* ($Ra^* = 0.083$ u, $T_m^* = 0.055$ u, $C^* = 0.783$ u, $f^* = 0.582$ u).

The Pareto frontier for the ECAP-6 hardened aluminum workpiece (see Figure 12d) has the following sections. Section I, between point p_1 and point p_2 , corresponds to the following cutting conditions: $v_c = 200$ m/min, $a_p = 0.20$ mm, $f_r = 0.15 \dots 0.081$ mm/rev. Section II, between point p_2 and point p_3 , corresponds to the following cutting conditions: $v_c = 200 \dots 100$ m/min, $a_p = 0.20$ mm, $f_r = 0.081$ mm/rev. Section III, between point p_3 and point p_4 , corresponds to the following cutting conditions: $v_c = 100$ m/min, $a_p = 0.20$ mm, $f_r = 0.081 \dots 0.045$ mm/rev. Section IV, between points p_4 and p_5 , corresponds to the following cutting conditions: $v_c = 100$ m/min, $a_p = 0.20$ mm, $f_r = 0.045 \dots 0.012$ mm/rev. p_3 is a special point on the Pareto curve. These points correspond to absolute minimum of the length of vector f^* ($Ra^* = 0.115$ u, $T_m^* = 0.066$ u, $C^* = 0.970$ u, $f^* = 0.715$ u).

3.6. Establishment of Optimum Turning Conditions

The optimum turning conditions may now be established, which involves narrowing the set of Pareto optimal decisions to a set of Pareto non-dominated decisions. For this purpose, the method of expert assessments was used to establish the lower importance of the dimensionless criterion of surface roughness as compared to the machining time for unit volume removal, T_m^* , and the cost

price of processing, C^* . As a result, Pareto non-dominated estimates are presented by the shortest three-dimensional vectors, f , located above the blue ones and at the angles of 17° , 14° , 8° , and 9° to the plane, f_3f_2 , for the ET-500 aluminum alloy workpieces, hardened by the ECAP-2, ECAP-4, and ECAP-6 processes, respectively (Figure 13a–d). The end points of these vectors coincided with point 4 on the Pareto curve for the aluminum workpiece obtained with ET-500 extrusion, with point 3 on the Pareto curve for the ECAP-2 hardened aluminum workpiece, with point 5 on the Pareto curve for the ECAP-4 hardened aluminum workpiece and with point 3 on the Pareto curve for the ECAP-6 hardened aluminum workpiece. They turned out to be the global minima in the case of unconditional optimization with the relation of importance $f_1:f_2:f_3 = 1.0:0.5:3.6$ (for the aluminum workpiece obtained with ET-500 extrusion), $f_1:f_2:f_3 = 1.0:5.2:0.6$ (ECAP-2 hardening), $f_1:f_2:f_3 = 1.0:9.0:0.6$ (ECAP-4 hardening) and $f_1:f_2:f_3 = 1.0:8.4:0.6$ (ECAP-6 hardening). With the actual coordinates, the global minimum corresponds to $Ra = 0.231 \mu\text{m}$, $T_m = 0.416 \text{ min/cm}^3$, $C = 7.223 \text{ \$}$, $v_c = 200 \text{ m/min}$, $a_p = 0.2 \text{ mm}$, $f_r = 0.045 \text{ mm/rev}$ (the case of obtaining an AA6061 workpiece with ET-500 extrusion), $Ra = 0.269 \mu\text{m}$, $T_m = 0.541 \text{ min/cm}^3$, $C = 12/074 \text{ \$}$, $v_c = 200 \text{ m/min}$, $a_p = 0.2 \text{ mm}$, $f_r = 0.045 \text{ mm/rev}$ (ECAP-2 hardening), $Ra = 0.199 \mu\text{m}$, $T_m = 0.458 \text{ min/cm}^3$, $C = 16/161 \text{ \$}$, $v_c = 150 \text{ m/min}$, $a_p = 0.25 \text{ mm}$, $f_r = 0.045 \text{ mm/rev}$ (ECAP-4 hardening) and $Ra = 0.267 \mu\text{m}$, $T_m = 0.549 \text{ min/cm}^3$, $C = 20.020 \text{ \$}$, $v_c = 100 \text{ m/min}$, $a_p = 0.2 \text{ mm}$, $f_r = 0.081 \text{ mm/rev}$ (ECAP-6 hardening).

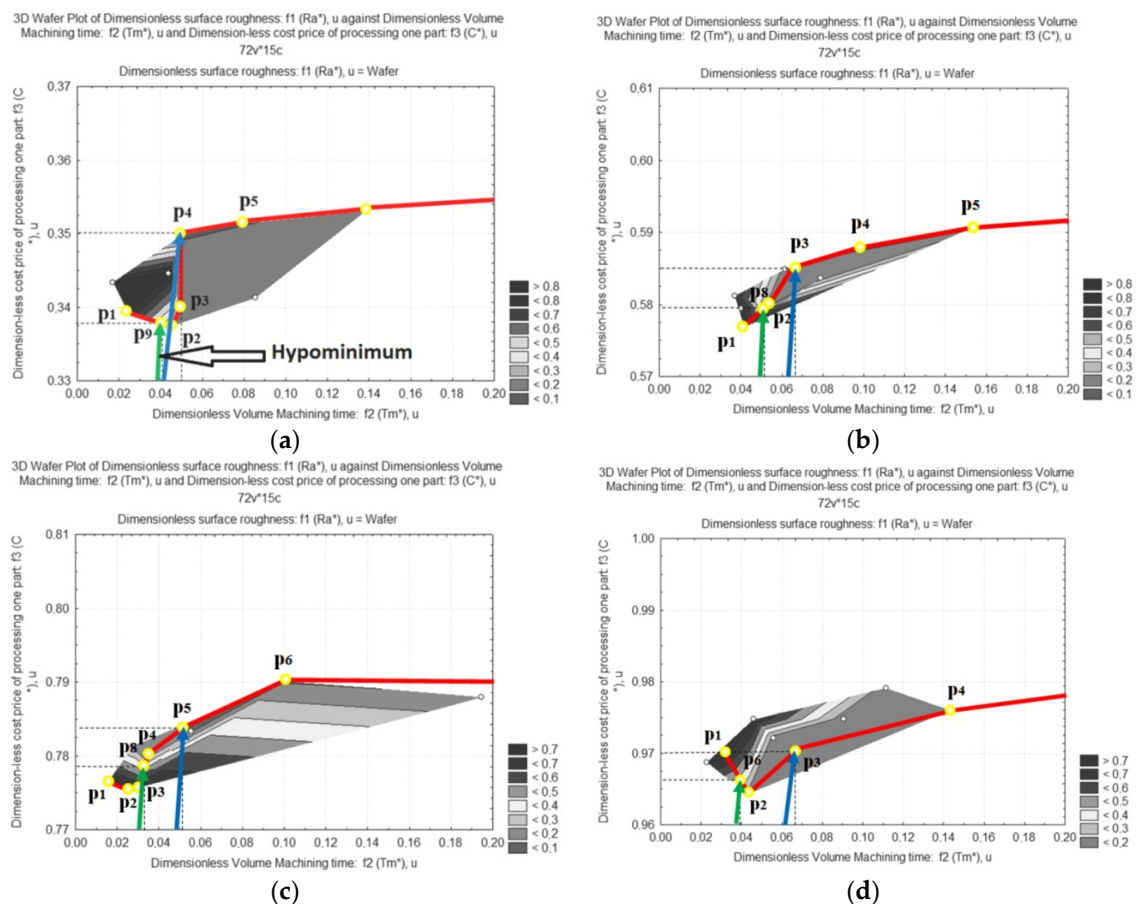


Figure 13. Global and local minima on the Pareto curve for the AA6061 aluminum workpiece: (a) obtained with ET-500 extrusion; (b) for the ECAP-2 hardened workpiece; (c) for the ECAP-4 hardened workpiece; (d) for the ECAP-6 hardened workpiece.

After imposing additional restrictions, namely the requirements of the design documentation, the minimum acceptable surface roughness value was established. It corresponded to $0.800 \mu\text{m}$ or the following points on the Pareto curves: p_9 (0.330; 0.041; 0.337; 0.485) in Figure 13a), p_8 (0.330; 0.051;

0.579; 0.554) in Figure 13b, p_8 (0.330; 0.031; 0.778; 0.667) in Figure 13c, and p_6 (0.330; 0.039; 0.966; 0.785) in Figure 13d. In this case, the valid relation of importance of the optimization criteria (the green vectors of estimates) become: for the aluminum workpiece obtained with ET-500 extrusion, $Ra^*/T_m^*/C^* = 1.0:0.1:2.3$, and for points p_4 and p_9 , the valid preference was $x_9 > x_4$ and the induced preference was $x_9 > x_4$; for the ECAP-2 hardened aluminum workpiece, $Ra^*/T_m^*/C^* = 1.0:0.2:2.3$, and for points p_3 and p_8 , the valid preference was $y_8 > y_3$ and the induced preference was $x_8 > x_3$; for the ECAP-4 hardened aluminum workpiece, $Ra^*/T_m^*/C^* = 1.0:0.1:2.4$, and for points p_8 and p_5 , the valid preference was $y_8 > y_5$ and the induced preference was $x_8 > x_5$; for the ECAP-6 hardened aluminum workpiece, $Ra^*/T_m^*/C^* = 1.0:0.1:2.9$, and for points p_3 and p_6 , the valid preference was $y_6 > y_3$ and the induced preference was $x_6 > x_3$.

As a result, the set of selected estimates Sel Y was limited to the green vectors, and the set of selected decisions, Sel X, to the three-dimensional vectors of the optimum cutting parameters for the workpiece obtained with ET-500 extrusion: $v_c = 200$ m/min, $a_p = 0.2$ mm, $f_r = 0.103$ mm/min, for the ECAP-2 hardened workpiece: $v_c = 200$ m/min, $a_p = 0.2$ mm, $f_r = 0.101$ mm/min, for the ECAP-4 hardened workpiece: $v_c = 143$ m/min, $a_p = 0.25$ mm, $f_r = 0.104$ mm/min; for the ECAP-6 hardened workpiece: $v_c = 200$ m/min, $a_p = 0.2$ mm, $f_r = 0.105$ mm/min.

In summary, it should be noted that the hypolocal optimum corresponded to the green vector estimates for the workpiece obtained with ET-500 extrusion without hardening (see Figure 13a).

4. Conclusions

- (1) For the first time, an investigation on both the cutting parameters (cutting speed and depth of cut, feed rate) and methods of hardening an AA6061 alloy workpiece (ET-500, ECAP-2, ECAP-4, ECAP-6) has been performed. Their complex effects have been modeled in terms of surface roughness (Ra) in finish turning, machining time for unit volume removal (T_m), and the cost price of processing one part (C) using a three-dimensional estimates vectors and artificial intelligence.
- (2) The effects of a dynamic hardening method on the microstructure and the properties of AA6061 have been investigated. The chip samples extruded at 500 °C had a grain size of 15.9 μm and the effect of 2, 4, and 6 ECAP passes caused grain refinement of about 5, 3.28, and 2.46 μm , respectively. This refinement was accompanied by an increase in microhardness from 41 HV to 110 HV, and an increase in the ultimate tensile strength from 132.4 to 403 Mpa.
- (3) Artificial neural networks in the form of an MLP 4-12-3 multilayer perceptron have provided the following accuracy in the predictions of the Ra , T_m , and C varies for an AA6061 workpiece: after ET-500 $\pm 0.82\%$, ECAP-2 $\pm 4.43\%$, ECAP-4 $\pm 1.95\%$, and ECAP-6 $\pm 1.17\%$ in the finish turning of a shaft with the diameter of 12 mm and length of 100 mm in the following cutting parameter ranges: cutting speed from 100 to 250 m/min, with a depth of cut from 0.25 to 1.0 mm, and a feed per revolution between 0.012 to 0.150 mm/rev.
- (4) Based on the surface relief-surface roughness, Ra , the effects of methods of dynamic hardening of an AA6061 alloy workpiece on the limits of Ra , T_m , and C values has been established. As compared to ET-500, ECAP-6 hardening decreased the minimum surface roughness by 76%, and the maximum by 8%; the minimum machining time needed to remove a unit volume remained unchanged, and the maximum increased by 6%; the minimum values of the cost price of processing one part increased 2.8-fold, and the maximum increased 3-fold. Hypominimal surface roughness can only be attained when using ECAP-6 hardening.
- (5) The hypolocal optimum in the turning of an AA6061 alloy workpiece has been established: the minimum length of a three-dimensional estimates vector with actual coordinates of $Ra = 0.800$ μm , $T_m = 0.341$ min/cm³, and $C = 6.955$ \$ corresponded to the optimum conditions of finish turning: cutting speed $v_c = 200$ m/min, depth of cut $a_p = 0.2$ mm, and feed per revolution $f_r = 0.103$ mm/rev (ET-500 extrusion without hardening).

Author Contributions: Conceptualization, A.T.A., D.Y.P. and I.N.E.; Methodology, A.T.A., D.Y.P. and I.N.E.; Software, I.N.E.; Validation, A.T.A., D.Y.P. and I.N.E.; Formal Analysis, A.T.A., D.Y.P. and I.N.E.; Investigation, A.T.A., M.A.T., M.M.E.R. and M.S.S.; Resources, A.T.A., M.M.E.R. and M.S.S.; Data Curation, A.T.A., D.Y.P. and I.N.E.; Writing—Original Draft Preparation, A.T.A., D.Y.P. and I.N.E.; Writing—Review & Editing, A.T.A., D.Y.P. and I.N.E.; Visualization, A.T.A., D.Y.P. and I.N.E.; Supervision, A.T.A., D.Y.P. and I.N.E.; Project Administration, A.T.A.; Funding Acquisition, A.T.A.

Acknowledgments: The authors extend their appreciation to the Deanship of Scientific Research at King Saud University for funding this work through research group No (RG-1439-020). The research was also supported through Act 211 of the Government of the Russian Federation under contract Nr 02.A03.21.0011.

Conflicts of Interest: The authors declare no conflict of interest.

References

- López De Lacalle, L.N.; Pérez-Bilbatua, J.; Sánchez, J.A.; Llorente, J.L.; Gutiérrez, A.; Albóniga, J. Using high pressure coolant in the drilling and turning of low machinability alloys. *Int. J. Adv. Manuf. Technol.* **2000**, *16*, 85–91. [[CrossRef](#)]
- Jurkovic, Z.; Cukor, G.; Andrejcek, I. Improving the surface roughness at longitudinal turning using the different optimization methods. *Teh. Vjesn.* **2010**, *17*, 397–402.
- Feldshtein, E.; Józwiak, J.; Legutko, S. The influence of the conditions of emulsion mist formation on the surface roughness of AISI 1045 steel after finish turning. *Adv. Sci. Technol. Res. J.* **2016**, *30*, 144–149. [[CrossRef](#)]
- Nouioua, M.; Yaltese, M.A.; Khettabi, R.; Belhadi, S.; Mabrouki, T. Comparative assessment of cooling conditions, including MQL technology on machining factors in an environmentally friendly approach. *Int. J. Adv. Manuf. Technol.* **2017**, *91*, 3079–3094. [[CrossRef](#)]
- Cantero, J.L.; Díaz-Álvarez, J.; Infante-García, D.; Rodríguez, M.; Criado, V. High speed finish turning of inconel 718 using PCBN tools under dry conditions. *Metals* **2018**, *8*, 192. [[CrossRef](#)]
- Mia, M.; Singh, G.; Gupta, M.K.; Sharma, V.S. Influence of Ranque-Hilsch Vortex Tube and Nitrogen Gas Assisted MQL in Precision Turning of Al 6061-T6. *Precis. Eng.* **2018**. [[CrossRef](#)]
- Fernández-Abia, A.I.; García, J.B.; López de Lacalle, L.N. High-performance machining of austenitic stainless steels. *Mach. Mach. Tools Res. Dev.* **2013**, 29–90. [[CrossRef](#)]
- Kovac, P.; Rodic, D.; Pucovsky, V.; Savkovic, B.; Gostimirovic, M. Application of fuzzy logic and regression analysis for modeling surface roughness in face milling. *J. Intell. Manuf.* **2013**, *24*, 755–762. [[CrossRef](#)]
- Wojciechowski, S.; Twardowski, P.; Pelic, M.; Maruda, R.W.; Barrans, S.; Krolczyk, G.M. Precision surface characterization for finish cylindrical milling with dynamic tool displacements model. *Precis. Eng.* **2016**, *46*, 158–165. [[CrossRef](#)]
- Karkalos, N.E.; Galanis, N.I.; Markopoulos, A.P. Surface roughness prediction for the milling of Ti-6Al-4V ELI alloy with the use of statistical and soft computing techniques. *Measurement* **2016**, *90*, 25–35. [[CrossRef](#)]
- Arnaiz-González, Á.; Fernández-Valdivielso, A.; Bustillo, A.; López de Lacalle, L.N. Using artificial neural networks for the prediction of dimensional error on inclined surfaces manufactured by ball-end milling. *Int. J. Adv. Manuf. Technol.* **2016**, *83*, 847–859. [[CrossRef](#)]
- Pimenov, D.Y.; Bustillo, A.; Mikolajczyk, T. Artificial intelligence for automatic prediction of required surface roughness by monitoring wear on face mill teeth. *J. Intell. Manuf.* **2018**, *29*, 1045–1061. [[CrossRef](#)]
- Hassui, A.; Diniz, A.E. Correlating surface roughness and vibration on plunge cylindrical grinding of steel. *Int. J. Mach. Tool Manuf.* **2003**, *43*, 855–862. [[CrossRef](#)]
- Sutowski, P.; Nadolny, K.; Kaplonek, W. Monitoring of cylindrical grinding processes by use of a non-contact AE system. *Int. J. Precis. Eng. Manuf.* **2012**, *13*, 1737–1743. [[CrossRef](#)]
- González, H.; Calleja, A.; Pereira, O.; Ortega, N.; López De Lacalle, L.N.; Barton, M. Super abrasive machining of integral rotary components using grinding flank tools. *Metals* **2018**, *8*, 24. [[CrossRef](#)]
- Niranjan, D.B.; Shivashankar, G.S.; Sreenivas Rao, K.V.; Praveen, R. Optimization of Cutting Process Parameters on AL6061 Using ANOVA and TAGUCHI Method. *Mater. Today Proc.* **2017**, *4*, 10845–10849. [[CrossRef](#)]
- Lazzaro, G.; Atzori, C. *Recycling of Aluminum Trimmings by Conform Process*; Minerals, Metals & Materials SOC (TMS): Warrendale, PA, USA, 1991; pp. 1379–1384.
- Gronostajski, J.; Matuszak, A. Recycling of metals by plastic deformation: An example of recycling of aluminium and its alloys chips. *J. Mater. Process. Technol.* **1999**, 92–93, 35–41. [[CrossRef](#)]

19. Risbood, K.A.; Dixit, U.S.; Sahasrabudhe, A.D. Prediction of surface roughness and dimensional deviation by measuring cutting forces and vibrations in turning process. *J. Mater. Process. Technol.* **2003**, *132*, 203–214. [[CrossRef](#)]
20. Svalina, I.; Sabo, K.; Šimunović, G. Machined surface quality prediction models based on moving least squares and moving least absolute deviations methods. *Int. J. Adv. Manuf. Technol.* **2011**, *57*, 1099–1106. [[CrossRef](#)]
21. Asiltürk, I. Predicting surface roughness of hardened AISI 1040 based on cutting parameters using neural networks and multiple regression. *Int. J. Adv. Manuf. Technol.* **2012**, *63*, 249–257. [[CrossRef](#)]
22. Azam, M.; Jahanzaib, M.; Wasim, A.; Hussain, S. Surface roughness modeling using RSM for HSLA steel by coated carbide tools. *Int. J. Adv. Manuf. Technol.* **2015**, *78*, 1031–1041. [[CrossRef](#)]
23. Acayaba, G.M.A.; Escalona, P.M.D. Prediction of surface roughness in low speed turning of AISI316 austenitic stainless steel. *CIRP J. Manuf. Sci. Technol.* **2015**, *11*, 62–67. [[CrossRef](#)]
24. Mia, M.; Dhar, N.R. Prediction of surface roughness in hard turning under high pressure coolant using Artificial Neural Network. *Measurement* **2016**, *92*, 464–474. [[CrossRef](#)]
25. Nieslony, P.; Krolczyk, G.M.; Wojciechowski, S.; Chudy, R.; Zak, K.; Maruda, R.W. Surface quality and topographic inspection of variable compliance part after precise turning. *Appl. Surf. Sci.* **2018**, *434*, 91–101. [[CrossRef](#)]
26. Jurkovic, Z.; Cukor, G.; Brezocnik, M.; Brajkovic, T. A comparison of machine learning methods for cutting parameters prediction in high speed turning process. *J. Intell. Manuf.* **2016**, 1–11. [[CrossRef](#)]
27. Mia, M.; Gupta, M.; Singh, G.; Krolczyk, G.; Pimenov, D.Y. An approach to cleaner production for machining hardened steel using different cooling-lubrication conditions. *J. Clean. Prod.* **2018**, *187*, 1069–1081. [[CrossRef](#)]
28. Sreejith, P.S. Machining of 6061 aluminium alloy with MQL, dry and flooded lubricant conditions. *Mater. Lett.* **2008**, *62*, 276–278. [[CrossRef](#)]
29. Anandakrishnan, V.; Mahamani, A. Investigations of flank wear, cutting force, and surface roughness in the machining of Al6061–TiB2 in situ metal matrix composites produced by flux-assisted synthesis. *Int. J. Adv. Manuf. Technol.* **2011**, *55*, 65–73. [[CrossRef](#)]
30. Ter Horst, R.; De Haan, M.; Gubbels, G.; Senden, R.; Van Venrooy, B.; Hoogstrate, A. Diamond turning and polishing tests on new RSP aluminium alloys. *Proc. SPIE Int. Soc. Opt. Eng.* **2012**, *8450*, 84502M. [[CrossRef](#)]
31. Islam, M.N. Effect of additional factors on dimensional accuracy and surface finish of turned parts. *Mach. Sci. Technol.* **2013**, *17*, 145–162. [[CrossRef](#)]
32. Cheng, Y.-C.; Hsu, W.-Y.; Abou-El-Hossein, K.; Olufayo, O.; Otieno, T. Investigation of diamond turning: Of rapidly solidified aluminum alloys. *Proc. SPIE Int. Soc. Opt. Eng.* **2014**, *9192*, 919214. [[CrossRef](#)]
33. Cheng, Y.-C.; Hsu, W.-Y.; Kuo, C.-H.; Abou-El-Hossein, K.; Otieno, T. Investigation of rapidly solidified aluminum by using diamond turning and a magnetorheological finishing process. *Proc. SPIE Int. Soc. Opt. Eng.* **2015**, *9575*, 957519. [[CrossRef](#)]
34. Kalyan, C.; Samuel, G.L. Cutting mode analysis in high speed finish turning of AlMgSi alloy using edge chamfered PCD tools. *J. Mater. Process. Technol.* **2015**, *216*, 146–159. [[CrossRef](#)]
35. Mkoiko, Z.; Abou-El-Hossein, K. Aspects of ultra-high-precision diamond machining of RSA 443 optical aluminium. *Proc. SPIE Int. Soc. Opt. Eng.* **2015**, *9575*, 95750A. [[CrossRef](#)]
36. Davoudinejad, A.; Ashrafi, S.A.; Niazi, A. Effect of tool wear on tri-phase CVD coated carbide tools life while turning Al6061. *Adv. Mater. Res.* **2012**, *488–489*, 457–461. [[CrossRef](#)]
37. Davoudinejad, A.; Ashrafi, S.A.; Barzani, M.M. Investigation into different tool coating performance while turning AL6061. *Adv. Mater. Res.* **2012**, *566*, 443–447. [[CrossRef](#)]
38. Hiremath, V.; Badiger, P.; Auradi, V.; Dundur, S.T.; Kori, S.A. Influence of particle size on Cutting Forces and Surface Roughness in Machining of B4Cp-6061 Aluminium Matrix Composites. *IOP Conf. Ser. Mater. Sci. Eng.* **2016**, *114*, 012041. [[CrossRef](#)]
39. Tootooni, M.S.; Liu, C.; Roberson, D.; Donovan, R.; Rao, P.K.; Kong, Z.J.; Bukkapatnam, S.T.S. Online non-contact surface finish measurement in machining using graph theory-based image analysis. *J. Manuf. Syst.* **2016**, *41*, 266–276. [[CrossRef](#)]
40. Zuperl, U.; Cus, F. Optimization of cutting conditions during cutting by using neural networks. *Robot. Comput. Integr. Manuf.* **2003**, *19*, 189–199. [[CrossRef](#)]

41. Gupta, A.K.; Guntuku, S.C.; Desu, R.K.; Balu, A. Optimisation of turning parameters by integrating genetic algorithm with support vector regression and artificial neural networks. *Int. J. Adv. Manuf. Technol.* **2015**, *77*, 331–339. [[CrossRef](#)]
42. Bouacha, K.; Terrab, A. Hard turning behavior improvement using NSGA-II and PSO-NN hybrid model. *Int. J. Adv. Manuf. Technol.* **2016**, *86*, 3527–3546. [[CrossRef](#)]
43. Mia, M.; Khan, M.A.; Rahman, S.S.; Dhar, N.R. Mono-objective and multi-objective optimization of performance parameters in high pressure coolant assisted turning of Ti-6Al-4V. *Int. J. Adv. Manuf. Technol.* **2017**, *90*, 109–118. [[CrossRef](#)]
44. Bataineh, O.; Dalalah, D. Strategy for optimising cutting parameters in the dry turning of 6061-T6 aluminium alloy based on design of experiments and the generalised pattern search algorithm. *Int. J. Mach. Mach. Mater.* **2010**, *7*, 39–57. [[CrossRef](#)]
45. Abbas, A.T.; Taha, M.A.; Ragab, A.E.; El-Danaf, E.A.; Abd El Aal, M.I. Effect of Equal Channel Angular Pressing on the Surface Roughness of Solid State Recycled Aluminum Alloy 6061 Chips. *Adv. Mater. Sci. Eng.* **2017**, 5131403. [[CrossRef](#)]
46. Ragab, A.E.; Taha, M.A.; Abbas, A.T.; Al Bahkali, E.A.; El-Danaf, E.A.; Aly, M.F. Effect of extrusion temperature on the surface roughness of solid state recycled aluminum alloy 6061 chips during turning operation. *Adv. Mech. Eng.* **2017**, *9*. [[CrossRef](#)]
47. Basak, S.; Dixit, U.S.; Davim, J.P. Application of radial basis function neural networks in optimization of hard turning of AISI D2 cold-worked tool steel with a ceramic tool. *Proc. Inst. Mech. Eng. B J. Eng. Manuf.* **2007**, *221*, 987–998. [[CrossRef](#)]
48. Karpat, Y.; Özel, T. Multi-objective optimization for turning processes using neural network modeling and dynamic-neighborhood particle swarm optimization. *Int. J. Adv. Manuf. Technol.* **2007**, *35*, 234–247. [[CrossRef](#)]
49. Yue, C.; Wang, L.; Liu, J.; Hao, S. Multi-objective optimization of machined surface integrity for hard turning process. *Int. J. Smart Home* **2016**, *10*, 71–76. [[CrossRef](#)]
50. Abbas, A.T.; Hamza, K.; Aly, M.F.; Al-Bahkali, E.A. Multiobjective optimization of turning cutting parameters for j-steel material. *Mater. Sci. Eng.* **2016**, *8*, 6429160. [[CrossRef](#)]
51. Abbas, A.T.; Pimenov, D.Y.; Erdakov, I.N.; Mikolajczyk, T.; El Danaf, E.A.; Taha, M.A. Minimization of turning time for high strength steel with a given surface roughness using the Edgeworth-Pareto optimization method. *Int. J. Adv. Manuf. Technol.* **2017**, *93*, 2375–2392. [[CrossRef](#)]
52. Abbas, A.T.; Pimenov, D.Y.; Erdakov, I.N.; Taha, M.A.; Soliman, M.S.; El Rayes, M.M. ANN Surface Roughness Optimization of AZ61 Magnesium Alloy Finish Turning: Minimum Machining Times at Prime Machining Costs. *Materials* **2018**, *11*, 808. [[CrossRef](#)] [[PubMed](#)]
53. Pourdavood, M.; Sedighi, M.; Asgari, A. ECAP process capability in producing a power transmission bimetallic rod. *Mater. Manuf. Process.* **2018**, *33*, 873–881. [[CrossRef](#)]
54. Rezaei, M.R.; Shabestari, S.G.; Razavi, S.H. Effect of ECAP consolidation process on the interfacial characteristics of Al-Cu-Ti metallic glass reinforced aluminum matrix composite. *Compos. Interface* **2018**, *25*, 669–679. [[CrossRef](#)]
55. Haase, M.; Khalifa, N.B.; Tekkaya, A.E.; Misiolek, W.Z. Improving mechanical properties of chip-based aluminum extrudates by integrated extrusion and equal channel angular pressing (iECAP). *Mater. Sci. Eng. A* **2012**, *539*, 194–204. [[CrossRef](#)]
56. Selmy, A.I.; El-Gohry, A.M.; Abd El Aal, M.I.; Taha, M.A. Characteristics of Solid State Recycling of Aluminum Alloy (AA6061) Chips by Hot Extrusion. *Int. Conf. Eng. Sci. Appl.* **2016**, *1*, 316–323.
57. Hu, M.; Ji, Z.; Chen, X.; Zhang, Z. Effect of chip size on mechanical property and microstructure of AZ91D magnesium alloy prepared by solid state recycling. *Mater. Charact.* **2008**, *59*, 385–389. [[CrossRef](#)]
58. Dash, M.; Liu, H. Consistency-based search in feature selection. *Artif. Intell.* **2003**, *151*, 155–176. [[CrossRef](#)]
59. Bergstra, J.; Bengio, Y. Random search for hyper-parameter optimization. *J. Mach. Learn. Res.* **2012**, *13*, 281–305.
60. Liu, Z.-G.; Ji, X.-H.; Liu, Y.-X. Hybrid non-parametric particle swarm optimization and its stability analysis. *Expert Syst. Appl.* **2018**, *92*, 256–275. [[CrossRef](#)]

